Performance Analysis of Opportunistic ARAIM for Navigation With GNSS Signals Fused With Terrestrial Signals of Opportunity

Mu Jia, *Graduate Student Member, IEEE*, Joe Khalife, *Student Member, IEEE*, and Zaher M. Kassas, *Senior Member, IEEE*

***Abstract*— Integrity monitoring of a vehicular navigation system that utilizes multi-constellation global navigation satellite systems (GNSS) signals fused with terrestrial signals of opportunity (SOPs) is considered. An opportunistic advanced receiver autonomous integrity monitoring (OARAIM) framework is developed to detect faults and calculate protection levels (PLs). The influence of fusing SOPs on the integrity performance is analyzed. It is shown that fusing a single SOP with GNSS signals essentially increases both the horizontal PL (HPL) and vertical PL (VPL), while fusing two or more SOPs could reduce the PLs and improves fault detection. Performance sensitivity analysis for the probability of SOP fault and user range error is conducted to characterize the fault-free HPL under different regimes. Experimental results on an unmanned aerial vehicle (UAV) navigating with GPS signals fused with cellular SOPs are presented to validate the effectiveness of the OARAIM framework and demonstrate the analysis of the integrity performance in the horizontal direction.**

***Index Terms*— Navigation, integrity, RAIM, protection level, GNSS, signals of opportunity.**

NOMENCLATURE

z_m^{G}	m-th GNSS pseudorange measurement.
$\boldsymbol{r}_{\mathrm{r}}$	Receiver's position vector.
$\boldsymbol{r}_m^{\mathrm{G}}$	m-th GNSS satellite postion vector.
$\delta t_{\mathrm{r},j}^{\mathrm{G}}$	Receiver's clock bias with respect to the i-th GNSS constellation's reference time.
v_m^{G}	Measurement noise for the m-th GNSS satellite.
$z_m^{\mathrm{G}'}$	GNSS pseudorange measurement before compensation.
$\hat{\delta}t^{\mathrm{G}}$	GNSS satellite's clock bias estimate.
$\hat{\delta}t_{\mathrm{iono}}$	Estimated ionospheric dalay.
$\delta t_{\mathrm{tropo}}$	Estimated troposheric delay.
$\boldsymbol{r}_n^{\mathrm{S}}$	Position of n-th SOP transmitter.
$\bar{\delta}t_{\mathrm{r}}$	SOP receiver's clock bias.
δt_n^{S}	Clock bias of the n-th SOP transmitter.
$\bar{v}_n^{\mathrm{S}}$	SOP pseudorange measurement noise.
$\delta t_{\mathrm{r},j}^{\mathrm{S}}$	SOP receiver's clock bias with respect to the j-th SOP subgroup (constellation).
$\delta t_{n,0}^{\mathrm{S}}$	Initial SOP clock bias.
N_{const}	Number of SOP constellations.
M_{const}	Number of GNSS constellations.
M_{s}	Number of GNSS satellites.
N_{s}	Number of SOP transmitters.
v_n^{S}	SOP pseudorange measurement noise in the re-parameterized measurement model.
$\boldsymbol{x}$	UAV state vector.
$\boldsymbol{z}$	Measurement vector.
$\mathbf{H}$	Measurement Jacobian matrix.
$\hat{\boldsymbol{x}}$	Estimated state vector.
$\mathbf{W}$	Wighting matrix in estimators.
$\hat{\boldsymbol{z}}^{(\infty)}$	Converged measurement prediction.
$\boldsymbol{y}$	Estimation residual vector.
$\mathbf{G}$	Geometry matrix.
$\mathbf{B}$	Measurement Jacobian associated with clock states.
el_l	Elevation angle.
az_l	Azimuth angle.
$d_{\mathrm{min}}^{\mathrm{S}}$	Minimum SOP horizontal distance.
$d_{\mathrm{max}}^{\mathrm{S}}$	Maximum SOP horizontal distance.
σ_{URA}	User Range Accuracy.
b_{nom}	Maximum nominal error.
P_{s}	Probability of single ranging source fault.
P_{const}	Probability of constellation-wide fault.
P_{thresh}	Integrity risk budget for unmonitored fault modes.
N_{f}	Number of fault modes to be monitored.
$P_{\mathrm{f}}^{(i)}$	Probability of fault mode i.
$\hat{\boldsymbol{x}}^{(i)}$	Fault-tolerant solution.
$\hat{\boldsymbol{x}}^{(0)}$	All-in-view solution.
$\Delta\hat{\boldsymbol{x}}^{(i)}$	Solution separation for the i-th fault mode.
$\mathbf{W}^{(i)}$	Integrity wighting matrix for fault mode i.
$\sigma_q^{(i)}$	Standard deviation of the i-th fault-tolerant navigation solution in the q-th directin.
$b_q^{(i)}$	Worst-case bias.
$\sigma_{ss,q}^{(i)}$	Standard deviation of solution separation.
$T_{i,q}$	Test threshold.

Manuscript received 8 April 2022; revised 4 November 2022 and 25 March 2023; accepted 3 May 2023. Date of publication 21 August 2023; date of current version 4 October 2023. This work was supported in part by the U.S. Department of Transportation (USDOT) through the Center for Automated Vehicle Research with Multimodal AssurEd Navigation (CARMEN) University Transportation Center (UTC) under Grant 69A3552047138 and in part by the National Science Foundation (NSF) under Grant 1929965. The Associate Editor for this article was S.-H. Kong. *(Corresponding author: Zaher M. Kassas.)*

Mu Jia and Zaher M. Kassas are with the Department of Electrical and Computer Engineering, The Ohio State University, Columbus, OH 43210 USA (e-mail: jia.641@osu.edu; zkassas@ieee.org).

Joe Khalife was with the Department of Mechanical and Aerospace Engineering, University of California, Irvine, CA 92697 USA. He is now with Apple, Cupertino, CA 95014 USA (e-mail: khalifej@uci.edu).

Digital Object Identifier 10.1109/TITS.2023.3277393

$\hat{x}_q^{(i)}$	Fault-tolerant solution in the q-th direction.
$\hat{x}_q^{(0)}$	All-in-view solution in the q-th direction.
P_{NM}	Probability of faults not monitored.
PL_q	Protection level in q-th direction.
$P_{\mathrm{FA\_H}}$	Coninuity budget in the horizontal direction.
$P_{\mathrm{FA\_V}}$	Coninuity budget in the vertical direction.
$PHMI_{\mathrm{H}}$	Integrity budget in the horizontal direction.
$PHMI_{\mathrm{V}}$	Integrity budget in the vertical direction.

I. Introduction

In safety-of-life navigation applications, e.g. aviation, the passenger and mission safety highly depends on the accuracy and reliability of the navigation system. This is particularly the case for civil aircraft autopilot systems, and unmanned aerial vehicles (UAVs), which are quickly becoming popular in a wide range of civilian and military applications [1]. Semi- and fully-automated autopilot systems, whether on ground or aerial vehicles, rely on global navigation satellite systems (GNSS) receivers and a suite of onboard sensors, e.g., radar, inertial navigation system (INS), etc. [2]. GNSS are relied upon to provide a navigation solution in a global frame and to correct for accumulating errors due to sensor dead reckoning.

While achieving higher levels of navigation accuracy has been a classic requirement, the trustworthiness in the navigation solutions, commonly assessed by navigation integrity, is evermore vital in safety critical applications. To ensure safe navigation, autopilot systems need to detect changes or anomalies in navigation signal characteristics that could affect the accuracy of the position calculated by the user equipment. Navigation systems need to tightly bound the position errors and ensure that the probability of position errors being not properly bounded is below a certain limit. However, current GNSS technologies are insufficient to support the full flight procedure, e.g., vertical guidance down to altitudes of 200 ft (LPV-200) [3]. To provide high-integrity navigation for UAVs and urban air mobility can be even more challenging, as these aerial vehicles may fly in urban environments, where GNSS signals are challenged and could be compromised via interference, jamming, or spoofing [4], [5].

Recently, terrestrial radio signals [6] have been shown to be an attractive alternative or supplement to GNSS signals [7], [8], either in an opportunistic manner, e.g., cellular signals [9], [10], digital television signals [11], [12], and FM radio signals [13], [14], or as radio beacons dedicated to navigation, e.g., Locata and NextNav [15]. While cellular base stations are already abundant in most locales, the number of base stations for future cellular generations keeps increasing dramatically, with the base station density of 5G projected to grow to 40-50 per km^2 [16]. Terrestrial signals of opportunity (SOPs) are particularly attractive for aerial integrity monitoring, as they can provide additional geometric diversity from below aerial vehicles [17].

Integrity monitoring relies on a priori knowledge of the nominal performance and fault rates of the ranging constellations. For GPS, the ground stations provide periodic updates regarding the safety-critical parameters contained in the Integrity Support Message (ISM). The safety-critical parameters include user range accuracy (URA) and user range error (URE), which are the standard deviations of the nominal errors used for integrity and continuity, respectively, and a priori probability of satellite failure. For SOPs and dedicated beacons, those parameters are either not fully characterized by enough data, or completely unknown. Hence, the impact of adding terrestrial signals with variable safety-critical parameters on integrity monitoring is still to be studied.

This paper conducts a thorough study on the impact of adding terrestrial measurements, whether from SOPs or dedicated beacons, with variable safety-critical parameters on GNSS-SOP integrity monitoring. It is shown that adding one SOP actually increases both the horizontal protection level (HPL) and vertical protection level (VPL). This happens when there is only one SOP available in the environment or the clocks of the SOPs are not synchronized (herein referred to as coming from different SOP constellations). In such cases, adding any SOP to the system would augment the state vector with an additional clock term, and the information from the additional SOP gets consumed in estimating the additional clock term. While the additional SOP is desirable from the perspective of improving the geometric diversity, it does not add redundancy in the measurements, and in fact, adds a vulnerability exhibited by an increase in the PLs. While new-generation cellular networks are evolving to support precise positioning, the current time synchronization requirement for both LTE and 5G is 3 μs [18], which corresponds to ranging errors of about 900 m. A recent study modeled, based on experimental data, the level of synchronization across cellular base stations [19]. This paper adopts such models and shows that adding two or more SOPs with synchronized clocks potentially reduces the HPL within a fairly large regime of safety-critical parameters.

This paper presents an opportunistic advanced receiver autonomous integrity monitoring (OARAIM) framework that utilizes multi-constellation GNSS signals fused with terrestrial SOPs, while detecting faults and calculating the PLs. The paper makes three contributions:

- It analytically shows that there needs to be at least two SOPs in an SOP constellation to possibly reduce PLs.
- It characterizes the horizontal integrity performance via extensive Monte Carlo simulations for adding a different number of SOPs with variable safety-critical parameters.
- It presents UAV experimental results demonstrating the efficacy of the proposed OARAIM to bound the integrity risk and comparing against the theoretical conclusions on the influence of adding terrestrial SOP measurements on HPL.

The remainder of this paper is organized as follows. Section II surveys related work about integrity monitoring and opportunistic navigation. Section III presents the navigation models, which include GNSS and SOP measurement models, weighted nonlinear least square (WLNS) estimator, and terrestrial SOP geometry model. Section IV presents the critical elements for OARAIM, namely definitions, safety-critical parameters and algorithm framework, which are foundational for the analysis in this paper. Section V analytically

proves that adding only one SOP in an additional constellation increases the PLs, indicating that to possibly improve navigation integrity, at least two or more SOPs are needed. Section VI presents the sensitivity analysis of integrity performance over variable SOP safety-critical parameters. Section VII discusses the experiment setup and results demonstrating the OARAIM framework. Section VIII concludes this paper by summarizing the analytical, simulation, and experimental results.

II. Related Work

The concept of navigation integrity, which measures the confidence of the information correctness provided by the navigation system. was introduced in the early 1990s to deal with safety threats caused by GPS faults in safety-critical missions [20]. The integrity information is provided by (i) external aiding systems, e.g. Ground Based Augmentation System (GBAS) [21] and Satellite Based Augmentation System (SBAS) [22]; (ii) onboard sensors, e.g. through the Airborne Based Augmentation System (ABAS). ABAS is usually referred as receiver autonomous integrity monitoring (RAIM), which is exceptionally attractive, as it is cost-effective and does not require building additional infrastructure [23]. RAIM for GPS constellation has been used since the mid-1990s. With the deployment of new GNSS constellations and the development of sensor technology, Advanced RAIM (ARAIM) has been proposed to account for multi-constellation GNSS measurements [24] (e.g. Galileo [25], GLONASS [26], and Beidou [27]), aiding sensors (e.g., INS-GPS [28], lidar-GNSS [29], and vision-GPS [30]). Since the introduction of ARAIM concept in the GPS Evolutionary Architecture Study (GEAS) phase II report [31], the cooperation between U.S. and E.U. on GPS/Galileo, through Working Group C Advanced Receiver Autonomous Integrity Monitoring Technical Subgroup (ARAIM SG), keeps improving the availability of safety-critical service, which is supposed to maintain integrity and continuity simultaneously [32]. As an extension to the original framework which only covers single-fault cases, [33] explicitly proposed the methods to compute the PLs for hypotheses with simultaneous faults. The estimator and detector design is optimized in [34] and [35] to minimize integrity risk in RAIM.

With the remarkable developments of BeiDou System (BDS) and GLONASS in the past decade, researcher has started to investigate utilizing multi-constellation ARAIM to meet more stringent integrity requirements. Foundational definitions, assertions, and assumptions for multi-constellation ARAIM are delicately checked and clarified for current RAIM-based operations [36]. The impact of incorporating more constellations to ARAIM on navigation performance is characterized, and a method of grouping multiple fault hypotheses to reduce high computational load caused by increasing number of measurements is proposed in [37]. The sensitivity of availability in response to changes in error model parameters is analyzed for multi-constellation ARAIM [38].

While GNSS has monopolized global navigation for decades, researchers have been working on developing new radionavigation systems and exploiting ambient signals for positioning. Opportunistic navigation has been widely studied over the last two decades [39], [40], [41], [42]. SOPs are exploited to provide a navigation solution in a global frame in a standalone fashion [43], [44] or could be used as aiding sources to dead reckoning sensors (e.g., lidar [45] and INS [46]). Among the different types of terrestrial SOPs, cellular signals are particularly attractive due to their inherent attributes: abundance, desirable geometric and spectral diversity, high received power, and large bandwidth. Cellular signals have shown high ranging and localization accuracy even in multipath environments [47], [48], [49], [50], [51] and on high-altitude aircraft [52], [53]. Recently, 5G signals have been studied for navigation purposes [54], [55], [56], and have been demonstrated on UAVs and ground vehicles [57], [58]. [59] develops a framework to exploit the entire bandwidth for navigation by using both "always-on" and "on-demand" reference signals. Recent studies have exploited terrestrial SOPs to enhance integrity monitoring performance by fusing GPS signals with SOPs. which has been shown to achieve improvement of integrity, in terms of PLs, over GPS-only for both aerial and ground vehicles [17], [60], [61]. However, the analyses are based on preliminary signal characterization and/or assumptions on safety-critical parameters of SOPs [62], [63]. On one hand, the SOP URE value in [17] is adopted based on signal characterization from a few hours worth of collected data, which is insufficient in the strict context of integrity. On the other hand, [61] assumed the SOP probability of fault to be 10 times that of GPS.

While multi-constellation GNSS ARAIM and opportunistic navigation has been extensively studied, the analyses do not directly apply to GNSS-SOP integrity monitoring. This is because: (i) terrestrial SOP transmitters have different geometry than GNSS satellites. Instead of orbiting above aerial vehicles, terrestrial SOPs usually are located below aerial vehicles; (ii) the safety-critical parameters of SOPs could have different order of magnitudes than those of GNSS.

III. Navigation Model Description

This section describes the pseudorange measurement models of the GNSS satellites and terrestrial SOPs and the WNLS estimator used to estimate the receiver's position. Furthermore, the terrestrial SOP geometry model used for the OARAIM performance analysis is presented.

A. GNSS Pseudorange Measurement Model

The aerial vehicle-mounted receiver makes pseudorange measurements to M_{s} GNSS satellites from M_{const} GNSS constellations. Let $i \in \{1, \ldots, M_{\mathrm{const}}\}$ denote the index of the constellation to which the m-th GNSS satellite belongs. The m-th GNSS pseudorange measurement from the i-th GNSS constellation at time-step k, after compensating for ionospheric delays, tropospheric delays, and the satellite's clock bias, is modeled as [64]

$$z_m^{\mathrm{G}}(k) = \|\boldsymbol{r}_{\mathrm{r}}(k) - \boldsymbol{r}_m^{\mathrm{G}}(k)\|_2 + c \cdot \delta t_{\mathrm{r},i}^{\mathrm{G}}(k) + v_m^{\mathrm{G}}(k), \quad (1)$$

where $z_m^{\mathrm{G}}(k) = z_m^{\mathrm{G}'}(k) + c\hat{\delta}t_m^{\mathrm{G}}(k) - c \cdot \hat{\delta}t_{\mathrm{iono}}(k) - c \cdot \hat{\delta}t_{\mathrm{tropo}}(k)$; $z_m^{\mathrm{G}'}(k)$ is the pseudorange from the m-th GNSS satellite before

compensation; c is the speed of light; $\hat{\delta t}^{\mathrm{G}}_m(k)$ is the m-th GNSS satellite's clock bias estimate; $\hat{\delta t}_{\mathrm{iono}}(k)$ and $\hat{\delta t}_{\mathrm{tropo}}(k)$ are the estimated ionospheric and tropospheric delays, respectively; $\boldsymbol{r}_{\mathrm{r}}(k)$ and $\boldsymbol{r}^{\mathrm{G}}_m(k)$ are the receiver and m-th satellite's three-dimension (3D) position vectors, respectively; $\delta t^{\mathrm{G}}_{\mathrm{r},i}(k)$ is the receiver's clock bias with respect to the i-th GNSS constellation's reference time; and v^{G}_m is the lumped noise term including residual ionospheric errors, which is modeled as a zero-mean, white Gaussian sequence with standard deviation σ^{G}_m.

B. Terrestrial SOP Pseudorange Measurement Model

The aerial vehicle-mounted receiver also makes pseudorange measurements from N_{s} terrestrial SOP transmitters, which are assumed to be stationary with known positions. Unlike GNSS satellites that transmit their clock parameters from which their clock error states can be deduced, terrestrial SOPs may not transmit any information about their clock error states. The n-th SOP measurement at time-step k can be modeled as

$$\bar{z}^{\mathrm{S}}_n(k) = \|\boldsymbol{r}_r(k) - \boldsymbol{r}^{\mathrm{S}}_n(k)\|_2 + c\cdot[\bar{\delta t}_{\mathrm{r}}(k) - \delta t^{\mathrm{S}}_n(k)] + \bar{v}^{\mathrm{S}}_n(k), \tag{2}$$

where $\boldsymbol{r}^{\mathrm{S}}_n(k)$ and $\delta t^{\mathrm{S}}_n(k)$ are the 3D position and clock bias of the n-th SOP transmitter, respectively; $\bar{\delta t}_{\mathrm{r}}(k)$ is the SOP receiver's clock bias with respect to the true time; and $\bar{v}^{\mathrm{S}}_n$ is the measurement noise, which is modeled as a zero-mean white Gaussian sequence with standard deviation $\bar{\sigma}^{\mathrm{S}}_n$.

The recent study [19] concluded that there exists a certain level of clock synchronization between cellular transmitters, i.e., the clock biases of different neighboring transmitters are dominated by one common term, due to the synchronization of the cellular network, leading to the model

$$c\cdot[\bar{\delta t}_{\mathrm{r}}(k) - \delta t\ldots\ldots\mathrm{S}_n(k)] = c\delta t^{\mathrm{S}}_{\mathrm{r}}(k) + c\delta t^{\mathrm{S}}_{0,n} + \epsilon_n(k), \tag{3}$$

where $c\delta t^{\mathrm{S}}_{\mathrm{r}}(k)$ is a common term driving the difference between the receiver and a subgroup of SOP clock biases, and $\epsilon_n(k)$ is an error term modeled as a zero-mean Gaussian random variable with variance $\sigma^2_{\epsilon_n}$. The initial biases $\left\{c\delta t^{\mathrm{S}}_{0,n}\right\}_{n=1}^{N_{\mathrm{s}}}$ can be obtained knowing the initial receiver position and given the initial measurement $\bar{z}^{\mathrm{S}}_n(0)$ according to $c\delta t^{\mathrm{S}}_{0,n} \approx \bar{z}^{\mathrm{S}}_n(0) - \|\boldsymbol{r}_r(0) - \boldsymbol{r}^{\mathrm{S}}_n(0)\|_2$. The initial receiver position can be estimated from GNSS measurements during a pre-calibration stage or before GNSS is cut off. The details of this calibration method can be found in [65].

A subgroup of SOPs whose clock biases are driven by a common term can be considered as an SOP constellation. This could happen when the transmitters have the same transmission protocol and are from the same network provider. Suppose that the SOPs can be grouped into N_{const} subgroups. i.e., SOP constellations. Let $j \in \{1,\ldots,N_{\mathrm{const}}\}$ denote the index of the constellation to which the n-th SOP belongs. After initial bias calibration, the n-th SOP pseudorange measurement $z^{\mathrm{S}}_n(k)$ can be remodeled as

$$z^{\mathrm{S}}_n(k) = \|\boldsymbol{r}_r(k) - \boldsymbol{r}^{\mathrm{S}}_n(k)\|_2 + c\delta t^{\mathrm{S}}_{\mathrm{r},j}(k) + v^{\mathrm{S}}_n(k), \tag{4}$$

where $c\delta t^{\mathrm{S}}_{\mathrm{r},j}(k)$ is the receiver's clock bias with respect to the j-th SOP subgroup's common reference time and the lumped measurement noise for the re-parameterized pseudorange measurement $v^{\mathrm{S}}_n(k) \triangleq \epsilon_n(k) + \bar{v}^{\mathrm{S}}_n(k)$ is modeled as a white Gaussian sequence with variance $\sigma^2_{\epsilon_n} + \sigma^{\mathrm{S}^2}_n$.

Equations (2) and (4) represent two different ways of modeling SOP pseudorange measurements. The grouping of SOPs in equation (4) enables the receiver to use a static estimator (e.g., WNLS) to estimate the position of the aerial vehicle. It is worth noting that the measurement error terms in the two models are modeled differently, hence, the noise variances should be characterized differently according to the two models. For cellular SOPs, a preliminary characterization of measurement errors was carried out in [17] by overbounding the error distribution of the experimentally recorded data over a period of 24 hours using DeCleene's single cdf-overbounding approach [66].

C. Navigation Solution

The receiver estimates its position vector using GNSS and SOP pseudorange measurements along with the GNSS and SOP receivers' biases vectors via a WNLS. The vector to be estimated is given by

$$\boldsymbol{x}(k) \triangleq \left[\boldsymbol{r}_r(k), c\boldsymbol{\delta t}^{\mathrm{G}^{\mathsf{T}}}(k), c\boldsymbol{\delta t}^{\mathrm{S}^{\mathsf{T}}}(k)\right]^{\mathsf{T}},$$

where

$$c\boldsymbol{\delta t}^{\mathrm{G}}(k) = \left[c\delta t^{\mathrm{G}}_1(k),\ldots,c\delta t^{\mathrm{G}}_{M_{\mathrm{const}}}(k)\right]^{\mathsf{T}},$$
$$c\boldsymbol{\delta t}^{\mathrm{S}}(k) = \left[c\delta t^{\mathrm{S}}_1(k),\ldots,c\delta t^{\mathrm{S}}_{N_{\mathrm{const}}}(k)\right]^{\mathsf{T}}$$

The time argument is omitted in the following for compactness of notation. The all-in-view combined GNSS-SOP measurement vector can be formed according to

$$\boldsymbol{z} \triangleq \left[z^{\mathrm{G}}_1,\ldots,z^{\mathrm{G}}_{M_{\mathrm{s}}},z^{\mathrm{S}}_1,\ldots,z^{\mathrm{S}}_{N_{\mathrm{s}}}\right]^{\mathsf{T}}.$$

A WNLS is then iterated to obtain an estimate of $\boldsymbol{x}$, denoted by $\hat{\boldsymbol{x}}$, using $\boldsymbol{z}$. Let h denote the iteration number, $\hat{\boldsymbol{x}}_h$ the estimate at iteration h, and $\hat{\boldsymbol{z}}_h$ the measurement prediction calculated using $\hat{\boldsymbol{x}}_h$. The all-in-view navigation solution update is obtained from the normal equations according to

$$\Delta\boldsymbol{x}_h = \left(\mathbf{H}^{\mathsf{T}}_h\mathbf{W}\mathbf{H}_h\right)^{-1}\mathbf{H}^{\mathsf{T}}_h\mathbf{W}\left(\boldsymbol{z} - \hat{\boldsymbol{z}}_h\right), \tag{5}$$

where $\mathbf{H}_h$ is the measurement Jacobian evaluated at $\hat{\boldsymbol{x}}_h$ and $\mathbf{W}$ is the weighting matrix. The weighting matrix is given by $\mathbf{W} = \mathbf{C}^{-1}_{\mathrm{acc}}$, where $\mathbf{C}_{\mathrm{acc}}$ is a diagonal matrix whose diagonal elements $\{\mathbf{C}_{\mathrm{acc}}(l,l)\}_{l=1}^{N_{\mathrm{s}}+M_{\mathrm{s}}}$ are the measurement noise variances used for continuity and accuracy. Details about $\mathbf{C}_{acc}$ can be found in Appendix A. The WNLS estimate at the $(h+1)$-th iteration is updated according to

$$\hat{\boldsymbol{x}}_{h+1} = \hat{\boldsymbol{x}}_h + \Delta\boldsymbol{x}_h,$$

and the iteration number is subsequently increased, i.e., $h \leftarrow h+1$. After convergence, the all-in-view navigation solution is denoted $\hat{\boldsymbol{x}}^{(\infty)}$, the measurement prediction after convergence

is denoted $\hat{\boldsymbol{z}}^{(\infty)}$, and the residual at convergence is denoted $\boldsymbol{y}$, which is defined as

$$\boldsymbol{y} \triangleq \boldsymbol{z} - \hat{\boldsymbol{z}}^{(\infty)}.$$

Let $\mathbf{H}$ denote the measurement Jacobian after convergence, which is an $(N_s + M_s) \times (3 + M_{\text{const}} + N_{\text{const}})$ matrix, that can be parameterized by the GNSS satellites and SOP transmitters' azimuth and elevation angles according to

$$\mathbf{H} \triangleq [\mathbf{G}, \mathbf{B}], \tag{6}$$

where $\mathbf{G}$ is the geometry matrix, and $\mathbf{B}$ is the time matrix. The l-th row of $\mathbf{G}$ matrix can be defined as

$$\mathbf{G}_l \triangleq [-c(el_l)s(az_l) \ -c(el_l)c(az_l) \ -s(el_l)],$$

where $c(\cdot)$ and $s(\cdot)$ denote the cos$(\cdot)$ and sin$(\cdot)$ functions, respectively; el_l and az_l are elevation angle and azimuth angle, respectively, of the l-th GNSS satellite or terrestrial SOP transmitter. The clock bias Jacobian can be expressed as

$$\mathbf{B} \triangleq \begin{bmatrix} \mathbf{B}^{\text{G}} & \mathbf{0}_{M_s \times N_{\text{const}}} \\ \mathbf{0}_{N_s \times M_{\text{const}}} & \mathbf{B}^{\text{S}} \end{bmatrix}, \tag{7}$$

where $\mathbf{B}^{\text{G}}$ is an $M_s \times M_{\text{const}}$ matrix denoting the GNSS clock bias Jacobian, whose m, i-th entry, denoted by $B_{m,i}$, is given by

$$B_{m,i} = \begin{cases} 1 & \text{if } m\text{-th satellite belongs to } i\text{-th constellation,} \\ 0 & \text{otherwise.} \end{cases}$$

$\mathbf{B}^{\text{S}}$ is measurement Jacobian associated with the SOP clock bias, which is defined similarly to $\mathbf{B}^{\text{G}}$.

D. Terrestrial SOP Geometry Model

To capture the randomness in the SOP transmitter locations, the terrestrial SOP network is modeled as a binomial point process (BPP) [67], [68], where the horizontal positions of N SOPs are independently and uniformly distributed over an annular region centered at the receiver, i.e., $\mathbb{B}_r(d^{\text{S}}_{\min}, d^{\text{S}}_{\max}) = \pi({d^{\text{S}}_{\max}}^2 - {d^{\text{S}}_{\min}}^2)$ [69], where $d^{\text{S}}_{\min}$ is the minimum horizontal distance required for the far-field assumption to hold and $d^{\text{S}}_{\max}$ is the maximum horizontal distance for which ranging signals can be detected by the receiver (Figure 1 (a) shows an example of an SOP realization for $N = 15$). The altitudes of the SOPs relative to the receiver are assumed to be uniformly distributed between $h^{\text{S}}_{\min}$ and $h^{\text{S}}_{\max}$. As shown in Figure 1(b), the location of the n-th SOP is represented by $(d^{\text{S}}_n, h^{\text{S}}_n, az^{\text{S}}_n)$, where d^{S}_n and h^{S}_n are the horizontal and vertical distances between the n-th SOP and the receiver, respectively, and az^{S}_n is the azimuth angle of the n-th SOP. As a result, the elevation angle of the n-th SOP el^{S}_n and the range to the n-th SOP r_{S_n} can be calculated as

$$el^{\text{S}}_n = \tan^{-1}\left(\frac{h^{\text{S}}_n}{d^{\text{S}}_n}\right),$$
$$r^{\text{S}}_n = \sqrt{{d^{\text{S}}_n}^2 + {h^{\text{S}}_n}^2}.$$

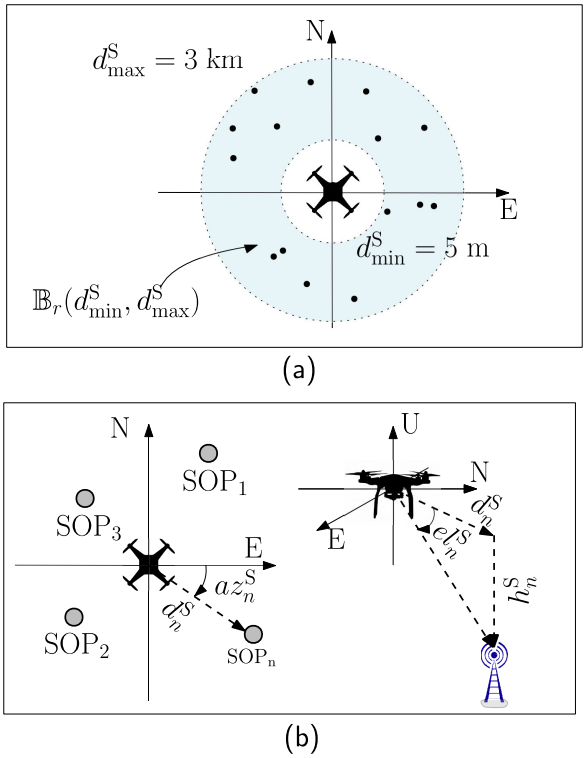

Fig. 1. (a) BPP realization with $N = 15$, in the angular region constrained by $d^{\text{S}}_{\min}$ and $d^{\text{S}}_{\max}$. The aerial vehicle is depicted in the center of the North-East frame. (b) Geometry of aerial vehicle-to-SOP. The aerial vehicle is the center of the North-East-Up frame.

IV. Critical Elements for OARAIM

This section presents the definitions, parameters, and algorithm framework for OARAIM, which are foundational for requirement and performance analysis. OARAIM is developed based on the baseline ARAIM [70], which is designed for GNSS navigation. Although ARAIM has the flexibility of incorporating multi-source measurements, it must be adapted when incorporating SOPs as discussed next.

A. Definitions for OARAIM

The definitions of key concepts, e.g., fault and nominal states, have been discussed and evolved based the of-the-time perspective of RAIM since the introduction of RAIM. However, integrity definitions for SOPs have not been explicitly made in the literature. In this subsection, the definitions for GNSS ARAIM are reviewed and the definitions for OARAIM are proposed thereafter. The definitions are discussed to provide foundations for the design and evaluation of the OARAIM algorithm. The discussion reveals that the conventions of defining transmitter performance allow for different definitions of integrity parameters. Therefore, the integrity parameters could take different values according to different ways of defining the transmitter performance. Most of the definitions are based on [71].

In terms of integrity, the characteristics of interest for navigation signals are mainly the nominal behavior and the probability that the signals might be in a faulty state. In OARAIM, there are four safety-critical parameters, inher-

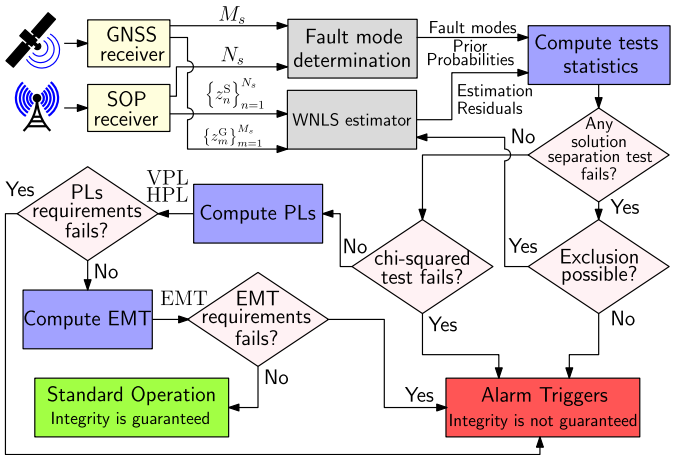

Fig. 2. OARAIM Flowchart. Note that M_S and N_S are the number of GNSS and SOP pseudoranges, respectively, and EMT denotes effective monitor threshold.

ited from the baseline ARAIM, that must be provided a priori to the user [24]:

- $\{\sigma_{\text{URA},m}\}_{m=1}^{M_s}$: URA, the standard deviation of a Gaussian distribution that overbounds the nominal clock and ephemeris error at the worst-case location on Earth, to be used for the determination of integrity. The parameter σ_{URA} is a conservative representation of the unfaulted error distribution.
- $\{b_{\text{nom},m}\}_{m=1}^{M_s}$: bound on the maximal bias affecting the nominal error of ranging source m to be used for the determination of integrity.
- $\{P_{\text{s},m}\}_{m=1}^{M_s}$: the probability that a ranging source m is faulty at a given time.
- $\{P_{\text{const},i}\}_{i=1}^{M_{\text{const}}}$: the probability of a constellation-wide fault.

The safety-critical parameters for GPS have been thoroughly characterized over the last several decades. The ARAIM SG provides values for URA, $b_{\text{nom},m}$, and probability of satellite and constellation fault for GNNS agreed by the groups. However, the values for the safety-critical parameters of SOPs have not been characterized due to limited adoption of these signals in safety-critical applications and the fact that one needs sufficient historical data to characterize these parameters, which has not materialized yet. Therefore, this paper will conduct a sensitivity analysis of performance on the safety-critical parameters for SOPs.

B. OARAIM Framework

This section presents the OARAIM framework introduced in [60] and [72] to incorporate GNSS pseudorange measurements and SOP pseudorange measurements. The solution separation tests and PL calculation are introduced to provide foundations for the analysis in later sections. OARAIM performs fault detection and exclusion (FDE) and PL calculation based on the multiple hypothesis solution separation (MHSS) algorithm [23]. Figure 2 shows the OARAIM algorithm flowchart.

OARAIM first determines the fault modes to monitor, based on the GNSS and SOP ranging sources visible to the receiver, so that the probability of fault modes other than the monitored ones is smaller than a predefined threshold P_{thresh}, i.e.,

$$1 - \sum_{i=0}^{N_{\text{f}}} P_{\text{f}}^{(i)} \leq P_{\text{thresh}}, \tag{8}$$

where N_{f} is the number of fault modes to be monitored and $P_{\text{f}}^{(i)}$ is the probability of fault mode i ($i \in \{1, \ldots, N_{\text{f}}\}$). For each fault mode, a fault-tolerant solution $\hat{\boldsymbol{x}}^{(i)}$ is defined as the navigation solution obtained from measurements excluding the hypothesized faulty measurements in the corresponding fault mode. The difference between the fault-tolerant solutions $\hat{\boldsymbol{x}}^{(i)}$ and the all-in-view solution $\hat{\boldsymbol{x}}^{(0)}$ serves as the test statistics for each alternative hypothesis. The difference vector for the i-th fault mode is computed as [70]

$$\Delta\hat{\boldsymbol{x}}^{(i)} = \hat{\boldsymbol{x}}^{(i)} - \hat{\boldsymbol{x}}^{(0)} = (\mathbf{S}^{(i)} - \mathbf{S}^{(0)})\boldsymbol{y}$$
$$\mathbf{S}^{(i)} = (\mathbf{H}^{\mathsf{T}}\mathbf{W}^{(i)}\mathbf{H})^{-1}\mathbf{H}^{\mathsf{T}}\mathbf{W}^{(i)}$$

where $\mathbf{W}^{(i)}$ is a diagonal weighting matrix, defined as

$$\mathbf{W}^{(i)}(l,l) = \begin{cases} \mathbf{C}_{\text{int}}^{-1}(l,l), & \text{if measurement } l \text{ is hypothesized faulty,} \\ 0, & \text{otherwise,} \end{cases}$$

where $\mathbf{C}_{\text{int}}$ is the diagonal covariance matrix characterizing the nominal error model used for integrity. Details about nominal error models used in OARAIM can be found in Appendix A.

Let the index $q \in \{1, 2, 3\}$ denotes the east, north, and up components, respectively. The variances of the q-th coordinate of i-th fault-tolerant navigation solution $\hat{x}_q^{(i)}$ are calculated as

$$\sigma_q^{(i)2} = (\mathbf{H}^{\mathsf{T}}\mathbf{W}^{(i)}\mathbf{H})_{q,q}^{-1}. \tag{9}$$

To bound the impact of the nominal bias for each measurement, $b_{\text{nom},j}$, on the position solutions, OARAIM calculates the worst-case bias for the every fault mode i. The worst-case bias can be given by

$$b_q^{(i)} = \sum_{l=1}^{M_{\text{s}}+N} \left|\mathbf{S}_{q,l}^{(i)}\right| b_{\text{nom},l}. \tag{10}$$

The variance of the difference $\Delta\hat{\boldsymbol{x}}^{(i)}$ between the all-in-view and the fault-tolerant position solutions is given by

$$\sigma_{\text{ss},q}^{(i)2} = \boldsymbol{e}_q^{\mathsf{T}}\left(\mathbf{S}^{(i)} - \mathbf{S}^{(0)}\right)\mathbf{C}_{\text{acc}}\left(\mathbf{S}^{(i)} - \mathbf{S}^{(0)}\right)^{\mathsf{T}}\boldsymbol{e}_q, \tag{11}$$

where $\boldsymbol{e}_q$ denotes the vector whose q-th entry is 1 and all other entries are 0, $\mathbf{C}_{\text{acc}}$ is the diagonal covariance matrix characterizing the nominal error model used for accuracy and continuity, whose details can be found in Appendix A.

The test threshold for the q-th coordinate of fault mode i is denoted by

$$T_{i,q} = K_{\text{fa},q}\sigma_{\text{ss},q}^{(i)}, \tag{12}$$

where

$$K_{\text{fa},1} = K_{\text{fa},2} = Q^{-1}\left(\frac{P_{\text{FA\_H}}}{4N_{\text{f}}}\right),$$
$$K_{\text{fa},3} = Q^{-1}\left(\frac{P_{\text{FA\_V}}}{2N_{\text{f}}}\right),$$

where $Q^{-1}(\cdot)$ is the inverse Q-function, and $P_{\text{FA\_H}}$ and $P_{\text{FA\_V}}$ are continuity budget allocated for false alarm in the horizontal and vertical direction, respectively. For each i and q, the solution separation test coefficient is defined by

$$\tau_{i,q} = \frac{|\hat{x}_q^{(i)} - \hat{x}_q^{(0)}|}{T_{i,q}}. \tag{13}$$

The solution separation test is conducted by testing $\tau_{i,q} \leq 1$ over all fault modes, i.e., $i \in \{1, \ldots, N_{\text{f}}\}$ and all directions, i.e., $q \in \{1, 2, 3\}$.

If any of the tests fails, the algorithm will try to perform fault exclusion. After the fault detection and exclusion is performed, the PL for each direction can be calculated. For HPL, the algorithm first computes PLs for the two horizontal directions, i.e., $q \in \{1, 2\}$, by solving the following equation [23]

$$2Q\left(\frac{PL_q - b_q^{(0)}}{\sigma_q^{(0)}}\right) + \sum_{i=1}^{N_{\text{f}}} P_{\text{f}}^{(i)} Q\left(\frac{PL_q - T_{i,q} - b_q^{(i)}}{\sigma_q^{(i)}}\right) = \frac{1}{2} PHMI_{\text{H}} \left(1 - \frac{P_{\text{NM}}}{PHMI_{\text{V}} + PHMI_{\text{H}}}\right), \tag{14}$$

where $Q(\cdot)$ is the Q-function; P_{NM} is the probability of the faults that are not included in the fault modes; and $PHMI_{\text{V}}$ and $PHMI_{\text{H}}$ are the integrity budget for the vertical and horizontal components, respectively. The HPL is calculated from

$$HPL = \sqrt{PL_1^2 + PL_2^2}. \tag{15}$$

The VPL can be calculated similarly by solving

$$2Q\left(\frac{PL_3 - b_3^{(0)}}{\sigma_3^{(0)}}\right) + \sum_{i=1}^{N_{\text{f}}} P_{\text{f}}^{(i)} Q\left(\frac{PL_3 - T_{i,3} - b_3^{(i)}}{\sigma_3^{(i)}}\right) = PHMI_{\text{V}} \left(1 - \frac{P_{\text{NM}}}{PHMI_{\text{V}} + PHMI_{\text{H}}}\right), \tag{16}$$

and $VPL = PL_3$.

Equations (8)-(14) for OARAIM are inherited from multi-constellation GNSS ARAIM. However, it is worth noting that a significant difference between multi-constellation GNSS ARAIM and OARAIM is that the definition of constellation in multi-constellation GNSS ARAIM is clear, while the grouping of SOPs and augmentation of system state space, i.e., adding a SOP 'constellation', depends on the relative synchronization of SOP clocks, as mentioned in Section III-B.

V. Analysis of Protection Level Reduction Due to Fusing SOPs With GNSS

This section analyzes the effect of fusing SOP pseudoranges with GNSS pseudoranges on the PL. It is shown that adding only one pseudorange measurement from an additional SOP constellation (i) reduces the fault detection sensitivity and (ii) increases the computed PLs over GNSS only. Therefore, to possibly improve integrity, there need to be at least two SOPs in the same constellation. The ARAIM is valid as long as the total number of pseudorange measurements is larger than the number of estimation states, so that the algorithm has measurement redundancy to perform solution separation [70]. However, the numerical study in [60] shows that adding only one SOP increases PLs. This paper extends the previous study by seeking analytical explanations of the performance degradation after adding only one SOP. Extending the analytical expressions derived in this section to two or more SOPs is analytically intractable. As such, Section VI resorts to Monte Carlo numerical simulations to show that the PL can be reduced under certain integrity parameters.

The case where only one pseudorange measurement from one SOP constellation arises if (i) there is only one SOP in the environment or (ii) the SOP does not share relative clock stability with other SOPs in the environment, as discussed in Section III-B. Recall that upon adding a single SOP, the state vector $\boldsymbol{x}$ is augmented with the SOP's corresponding additional clock state $c\delta_n^{\text{S}}$. It has been proved in [19] that adding one pseudorange measurement from an additional constellation does not improve the position estimate. Specifically, adding one pseudorange measurement from an additional constellation will change neither the position error nor the position error uncertainty. However, whether adding one SOP improves the integrity performance has not been studied. The following theorems show the influence of adding one SOP on the integrity performance, in terms of fault detection sensitivity and computed PLs, respectively.

Theorem 1: Consider M_{s} pseudorange measurements from M_{const} constellations in the ARAIM algorithm, where $M_{\text{s}} \geq 3 + M_{\text{const}}$. Assume that there exists another constellation to be used for ranging. Suppose that the probability of single and constellation-wide faults for the ranging sources is such that the maximum number of simultaneous faults to be monitored is 1. Adding one pseudorange measurement from an additional constellation will make the algorithm less sensitive to the faults of the original M_{s} measurements. Furthermore, the algorithm cannot detect faults from the additional measurement.

Proof. See Appendix C.

From Theorem 1, it can be implied that the number of SOP measurements in a constellation to benefit detection of GNSS fault is no less than 2. Furthermore, the number of SOP measurements in a constellation for faults in those SOPs being possibly detectable by OARAIM is no less than 2. The influence of adding one measurement from an additional constellation on the computed PLs is shown by the following theorem.

Theorem 2: Consider M_{s} pseudorange measurements from M_{const} constellations , where $M_{\text{s}} \geq 3 + M_{\text{const}}$ for the ARAIM algorithm to perform fault detection and compute PLs under baseline specifications. Assume that there exists another constellation to be used for ranging. Suppose that the probability of single and constellation-wide faults is such that the maximum number of simultaneous faults to be monitored is 1. Adding one pseudorange measurement from the additional constellation increases the vertical and horizontal protection levels.

Proof. See Appendix D.

As a demonstration of Theorem 2, Figure 3 shows the average PL reduction by adding one SOP with different probability of SOP fault over 5000 realizations of Monte Carlo simulation, whose setup is present in detail in the following

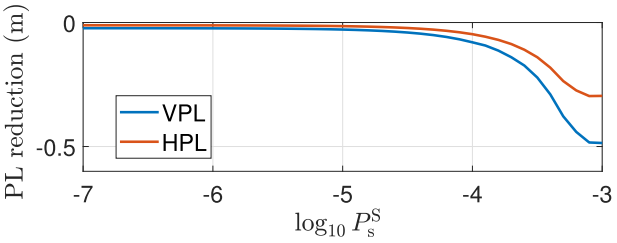

Fig. 3. Simulation result showing PL increases after adding one SOP with different P_s^S. Note that PL reduction denotes the PL after adding one SOP subtracted by the PL before adding the SOP.

section. From Figure 3, adding one SOP with different P_s^S always increases the PLs, which matches Theorem 2. It is worth noting that with larger P_s^S, the PL increase becomes larger, which is also declared by (32).

Note that Theorem 1 and Theorem 2 do not address the influence of adding $N_s \geq 2$ SOPs, while, however, is studied in Section VI via simulations.

VI. Fault-Free Integrity Performance Sensitivity Analysis

The impact of adding SOP measurements on the integrity performance is not completely obvious. On one hand, adding SOP measurements increases redundancy; hence, it presumably reduces the integrity risk. On the other hand, it is possible that adding more measurements increases the probability of hazardous misleading information (HMI), especially when the additional measurements have large probability of fault. Moreover, the safety-critical parameters are not fully characterized, which makes the impact of adding SOP measurements more difficult to track. As such, this section conducts simulation studies to characterize the integrity performance, specifically, HPL, upon incorporating SOPs with different assumptions of safety-critical characteristics, namely, σ_{URA}^S and P_s^S.

In order to quantify the integrity risk of the position solution and its error bound, a trusted model of the signals' safety-critical features is needed. However, these models for SOPs are not fully developed yet. From the integrity perspective, the navigation signal can be characterized by a nominal model and a model of potential threats. The nominal model describes the expected measurement error when no faults are present. The faults are by definition, instances where the nominal model is not valid. Based on the analyses in Section IV-A, the distinction between nominal and faulted conditions can be arbitrary. For example, one could choose to model common (but bounded) faults by inflating the nominal error model.

Besides that the fault condition can be "arbitrarily" defined, SOP signals have not been fully characterized by large-scale experimental campaigns (i.e., spanning very long duration and different environments). While an attempt to characterize the pseudorange error distribution has been made in [17], [62], this paper does not assume the availability of such characterization. Instead, the OARAIM performance is studied via Monte Carlo simulation for adding SOP, with varying safety-critical parameters, namely, σ_{URA}^S and P_s^S.

TABLE I
Simulation Setup

Parameter	Description	Value
I_{REQ}	Total integrity budget	10^{-7}
$PHMI_{\text{H}}$	Integrity budget allocated to vertical direction	9.9×10^{-8}
$PHMI_{\text{V}}$	Integrity budget allocated to horizontal direction	10^{-9}
$C_{\text{REQ,FA}}$	Continuity budget allocated to false alarm	10^{-7}
$P_{\text{FA\_H}}$	False alarm budget allocated to horizontal direction	9.9×10^{-8}
$P_{\text{FA\_V}}$	False alarm budget allocated to vertical direction	10^{-9}
P_{thresh}	Upper bound for the integrity risk from unmonitored faults	6×10^{-8}
$\{\sigma_{\text{URA},m}^{\text{GPS}}\}_{m=1}^{M_s}$	User range accuracy for GPS satellites	1 m
$\{b_{\text{nom},m}^{\text{GPS}}\}_{m=1}^{M_s}$	Nominal bias for GPS satellites	0.75 m
$\{P_{s,m}^{\text{GPS}}\}_{m=1}^{M_s}$	Narrow fault probability for GPS satellites	10^{-5}
$\{P_{s,n}^{\text{S}}\}_{n=1}^{N_s}$	Narrow fault probability for SOP transmitters	$[10^{-7}, 10^{-1}]$
$P_{\text{const}}^{\text{GPS}}$	GPS constellation fault probability	10^{-8}
$P_{\text{const}}^{\text{S}}$	SOP constellation fault probability	10^{-4}

In the simulation, terrestrial SOP pseudoranges are fused with GPS pseudoranges. This paper assumes a stationary receiver located in Orange County, California, USA. The receiver position is fixed at $\boldsymbol{r}_r = 10^6 \times [-2.482345, -4.700049, 3.513616]$, expressed in the Earth-Centered-Earth-Fixed (ECEF) frame. It is shown that the difference of integrity performance along the longitude direction is negligible [24]. The influence of the receiver's latitude is not the focus of this study. As such, this paper chooses to fix the receiver's position, while the geometric distribution of GPS satellites is varied by randomizing the time. As the nominal orbital period of a GPS satellite is 11 hours and 58 minutes, which is almost half of a sidereal day, one can randomly choose time in an approximately 24-hour interval to get GPS satellite positions, without having to randomize the date. Cellular SOP base stations are placed randomly based on the BPP model mentioned in the Section III-D.

Table I shows the OARAIM constants and inputs used in the simulation [70]. Note that this study employs LPV-200 requirements. P_s^S is varied from 10^{-7} to 10^{-1}, and σ_{URA}^S is varied from 0.5 to 25. For each combination of P_s^S and σ_S^S, there are 5000 Monte Carlo realizations. The 5000 Monte Carlo realizations uniformly span time of a day to obtain GPS

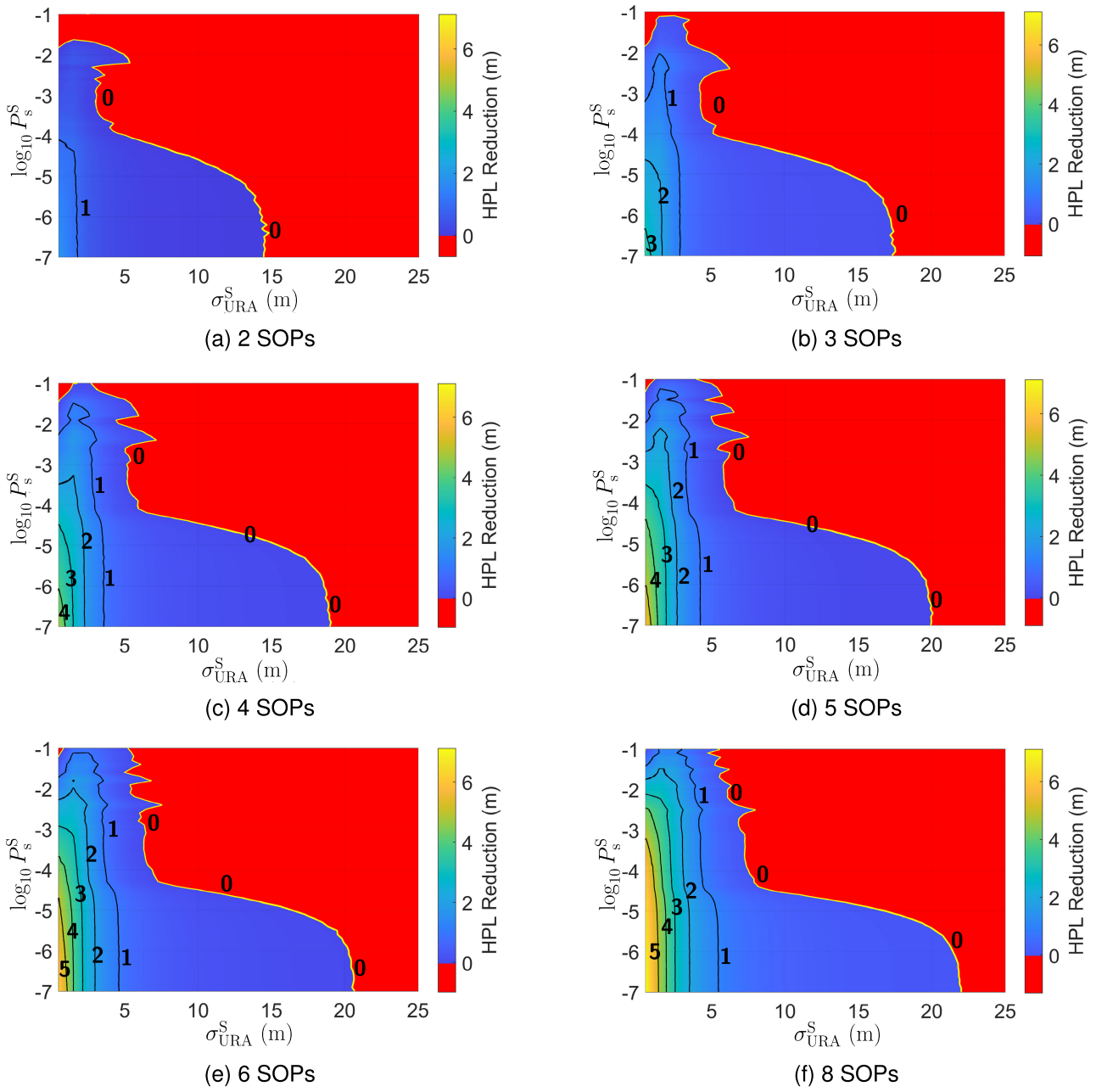

Fig. 4. Color map of HPL reduction for different $\sigma_{\mathrm{URA,SOP}}$ and P_S: (a) 2 SOPs; (b) 3 SOPs; (c) 4 SOPs; (d) 5 SOPs; (e) 6 SOPs; (f) 8 SOPs. The red region is where HPL reduction is below zero, indicating that HPL increases after adding SOPs, while other regions are where the HPL reduces after adding SOPs.

satellite position. Cellular transmitters are placed randomly based on the BPP model for each realization. The HPL reduction is calculated by averaging over the 5000 realizations. The sensitivity analysis results are shown in Figure 4. The following conclusions can be drawn from the simulation results: (i) adding no less than 2 "regular" SOPs (i.e., SOPs with reasonably small $\sigma_{\mathrm{URA}}^{\mathrm{S}}$ and $P_{\mathrm{s}}^{\mathrm{S}}$) will reduce the HPL; (ii) for two and more SOPs, with $P_{\mathrm{s}}^{\mathrm{S}}$ and $\sigma_{\mathrm{URA}}^{\mathrm{S}}$ increasing, the PL reduction decreases; (iii) with the number of SOPs increasing, the $\sigma_{\mathrm{URA}}^{\mathrm{S}}$ required for HPL reduction increases, which can be seen from that the boundary between positive and negative region of PL reduction moves to the right-hand side with more SOPs; and (iv) for the scenario of adding 2 SOPs with extremely large probability of fault, e.g., $P_{\mathrm{s}}^{\mathrm{S}} = 0.1$, the PL always increases, no matter how small $\sigma_{\mathrm{URA}}^{\mathrm{S}}$ is.

From Figure 4, it can be concluded that as number of SOPs increase, there will be less scenarios where adding SOPs degrades the performance. With enough SOPs, even signals with less favorable safety-critical characteristics (e.g., $\sigma_{\mathrm{URA}}^{\mathrm{S}}$ is 20 times larger than $\sigma_{\mathrm{URA}}^{\mathrm{GPS}}$ and $P_{\mathrm{s}}^{\mathrm{S}}$ is 100 times larger than $P_{\mathrm{s}}^{\mathrm{GPS}}$) would still reduce the HPL.

It is worth noting that the conclusions made in this section only apply to HPL. Terrestrial SOPs have relatively less geometric diversity in the vertical direction– they usually possess similar altitudes. The vertical integrity performance is sensitive to the SOPs' vertical geometric distribution and

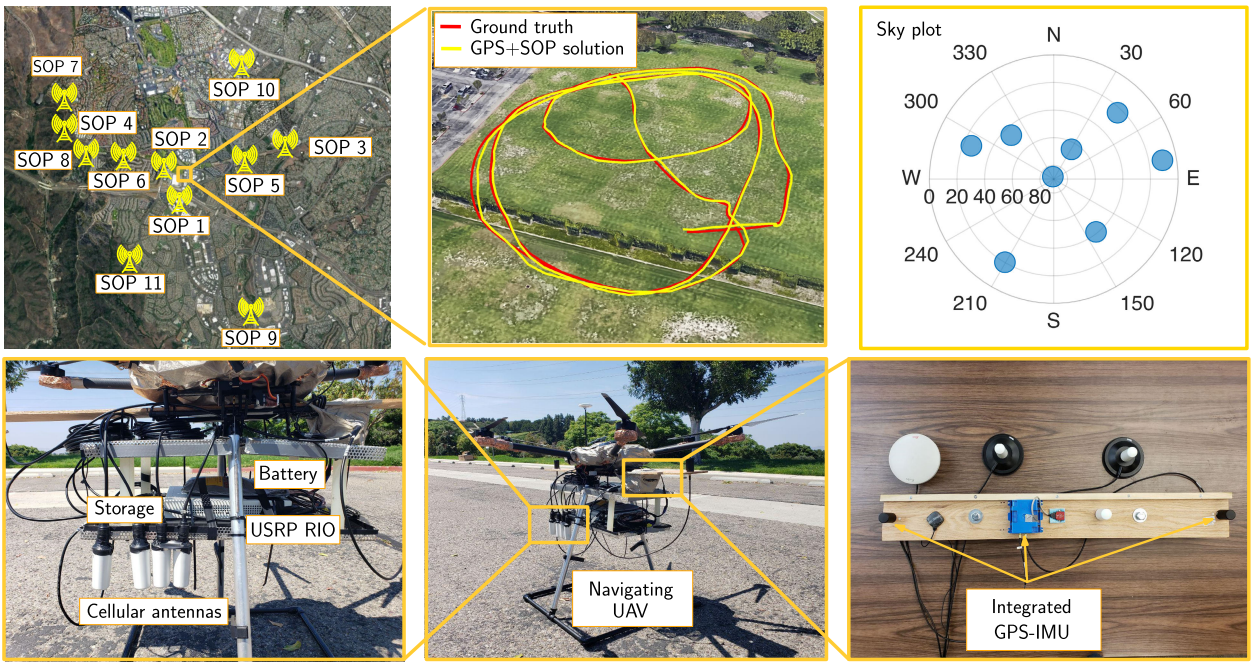

Fig. 5. Experimental hardware setup, navigation solution, and the traversed trajectory along with the position of cellular LTE SOP towers and the sky plot of GPS satellite positions.

their relative positions with respect to the receiver (e.g., a receiver may be located at the same altitude, higher, or lower than terrestrial SOPs, which is radically different than the relative geometry with respect to GNSS satellites). The influence of SOP geometry on the vertical integrity performance is not studied in this paper and is deferred to future work.

VII. Experimental Results

This section presents the experimental results on a UAV to demonstrate the proposed OARAIM framework and validate the sensitivity analysis of the integrity performance. First, Theorem 1 is demonstrated by showing detection sensitivity before and after adding one SOP pseudorange measurement over an experiment trajectory. Second, the experiment shows that the HPL bounds the horizontal position error (HPE) along the experiment trajectory, indicating OARAIM's ability to protect against integrity risk.

A. Experiment Setup

Figure 5 shows the environment and hardware setup for the experiment. A DJI Matrice 600 UAV was equipped with a dual-channel National Instrument (NI) universal software radio peripheral (USRP)-2955, driven by a GPS disciplined oscillator (GPSDO), to sample LTE SOPs. Four LTE carrier frequencies, 739, 1955, 2125, and 2145 MHz, were collected during the experiments. These frequencies are channels allocated for the U.S. cellular providers AT&T, T-Mobile, and Verizon. The sampling rate was set to 10 MSps and the sampled LTE signals were recorded on a laptop for post-processing. An LTE software-defined receiver (SDR) developed in [73] was used to process the sampled LTE signals to get the LTE pseudorange measurements.

The UAV was also equipped with a Septentrio AsteRx-i V, which has dual antenna multi-frequency GNSS receiver with RTK and a Vectornav VN-100 micro electromechanical systems (MEMS) inertial measurement unit (IMU). The integrated GNSS-IMU system provides both the raw GNSS measurements and ground-truth navigation solution. The raw GNSS measurements, after ionospheric and tropospheric corrections using Klobuchar Ionospheric Model and the Hopfield Tropospheric Model [74], and the LTE pseudorange measurements are fed into the WNLS estimator to calculate the GNSS-SOP coupled navigation solution. The integrity parameters are set the same as the simulation setup in Table I, except $\{P^{\mathrm{S}}_{\mathrm{s},n}\}_{n=1}^{N_s}$ is set to be 10^{-4}. As mentioned earlier, the probability of SOP fault has not been fully characterized nor agreed upon by standards bodies. The choice of $\{P^{\mathrm{S}}_{\mathrm{s},n}\}_{n=1}^{N_s}$ is only intended for the demonstration of the analytical and simulation results in this work.

The GPS and SOP pseudorange measurements were fed into the navigation framework discussed in Section III to produce the navigation solution and calculate the HPE. Over the course of the experiment, the UAV traversed a trajectory of 815 m in 220 s, while listening to 11 LTE towers. The locations of the towers in the environment were mapped prior to the experiment.

B. HPL Bounding

In this subsection, the ability of the OARAIM to bound the integrity risk, i.e., to bound the HPE with real-time HPLs, is validated. Over the course of the experiment, all GPS satellites above an elevation angle of 15° and all available SOPs were used to produce the navigation solution and compute HPLs. Figure 6 shows that HPE can always be bounded by real-time HPLs for the GPS+SOP framework.

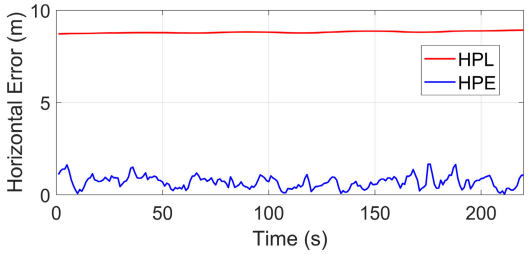

Fig. 6. HPE and corresponding HPL.

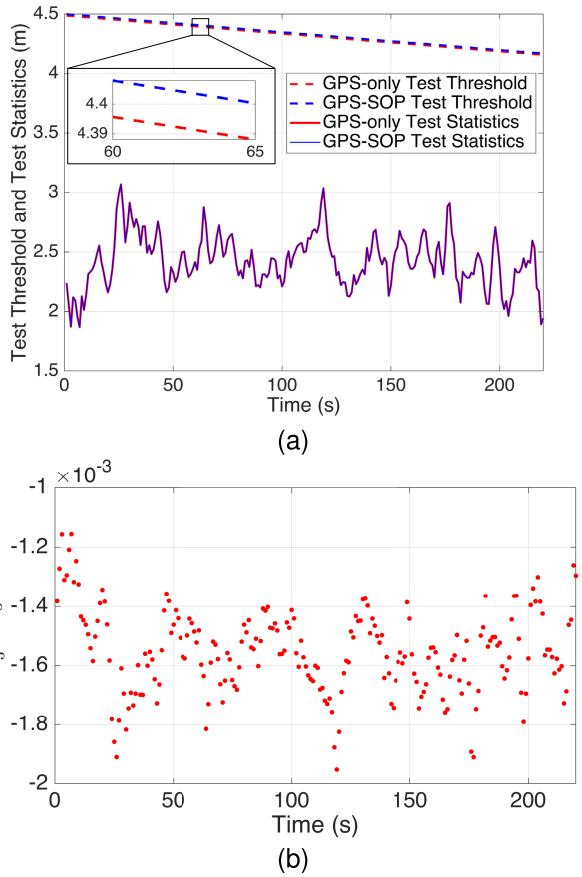

Fig. 7. Experiment results for fault detection corresponding to the GPS fault mode where GPS satellite with PRN number of 8 is faulty: (a) test threshold and statistics for GPS-only and GPS with one SOP, showing that adding one SOP does not change the test statistics while increases the test threshold; (b) the difference of test coefficients for the GPS fault mode between GPS-only and GPS with one SOP.

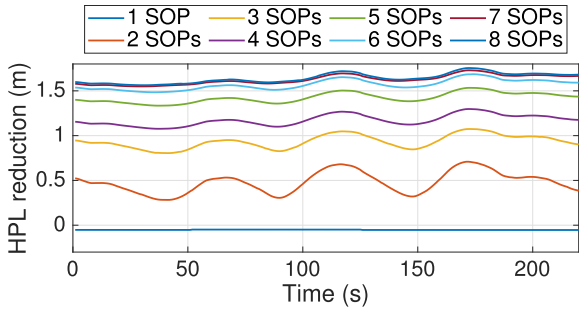

Fig. 8. HPL reduction for different numbers of SOPs over the experiment trajectory.

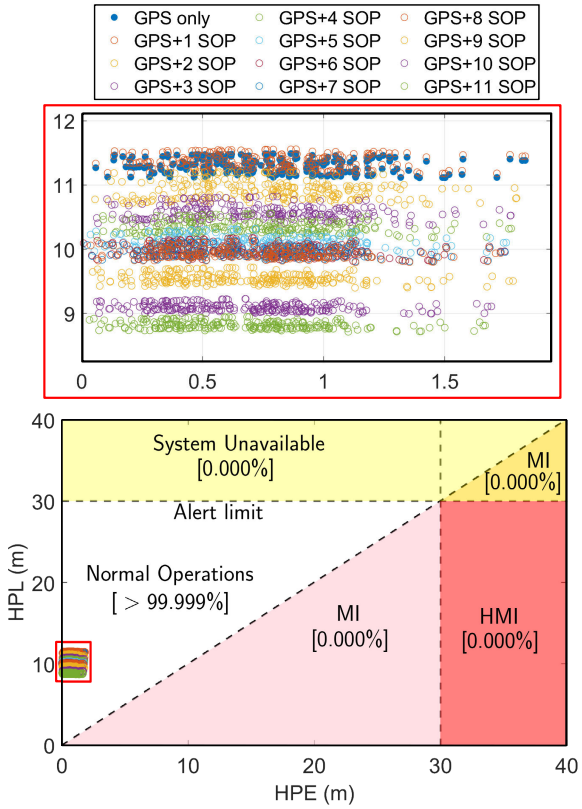

Fig. 9. The Stanford Diagram showing HPE and HPL for GPS only and GPS with different numbers of SOPs. On top is the zoom-in view of the data points. Note that MI denotes misleading information.

C. Detection Sensitivity

This subsection presents experimental results evaluating Theorem 1. This theorem was demonstrated by comparing the test statistics, thresholds, and coefficients for using GPS only pseudorange measurements and GPS pseudorange measurements with an additional SOP pseudorange measurement, i.e. SOP 1 shown in Figure 5. Figure 7(a) shows the test thresholds and statistics for the fault mode where the GPS satellite with PRN number of 8 is faulty. It is shown that adding one SOP from an additional constellation does not change the test statistics, whereas increases the test threshold. Figure 7(b) shows the test coefficient will be reduced by adding one additional SOP pseudorange measurement. This indicates that the detection sensitivity for GPS fault modes is reduced.

D. HPL Reduction for Adding SOPs

Next, the PL reduction after adding SOPs is demonstrated. Based on the common definition of narrow fault mentioned in Subsection IV-A, $P_s^S = 10^{-4}$ is chosen as a sample value in the experiment to compute HPLs for adding SOPs. As the experiment was conducted in a semi-urban area, σ_{URA}^S was chosen to be 3, which is the characterized value of semi-urban model from [17].

To calculate the HPL reduction, GPS-only HPL was first calculated and subtracted from the corresponding HPL for the GPS-SOP solution with different number of SOPs. The order of adding SOPs followed the numbering in Figure 5. Figure 8

shows the HPL reduction over the experiment course. One can see that adding one SOP slightly increases the HPL, which affirms Theorem 2. For two or more SOPs, the results show HPL reduction over the experiment trajectory. Note that results for only up tp 8 SOPs are plotted in Figure 5 to avoid the plot being discernible.

The Stanford Diagram, which expresses the working regime of the algorithm by the visualization of each epoch's HPL and HPE with respect to the alert limit, is plotted in Figure 9 for GPS only and GPS with different number of SOPs. There are a total of 2880 epochs, among which 100% are in the normal operations, which shows that OARAIM indeed meets the integrity requirement. One can also notice from the zoom-in view in Figure 9 that adding one SOP does not change the HPE, but it increases the HPL. Adding two or more SOPs reduces both the HPL and HPE.

VIII. Conclusion

This paper analyzed the integrity performance of OARAIM after incorporating terrestrial SOP measurements with variable safety-critical parameters. These analyses were conducted to support RAIM algorithm design for SOPs whose safety-critical parameters are not fully characterized with adequate historical data. First, the GNSS and SOP pseudorange measurement models were presented. In particular, two SOP pseudorange measurement model were proposed, one of which enables grouping of SOPs to support static estimators. Moreover, the OARAIM framework was proposed to incorporate SOPs with multi-constellation GNSS. The critical elements for OARAIM was also explicitly discussed. The least number of SOP pseudorange measurements to possibly improve integrity performance was proved to be no less than 2. This theoretical derivation also showed that to get integrity improvement with NLS-based ARAIM, the SOP pseudorange measurements need to be grouped into an SOP constellation. Then, the HPL reduction after adding different number of terrestrial SOPs with variable safety-critical parameters was analyzed through simulation. Finally, an experimental study was conducted to validate the OARAIM framework, theoretical study, and performance characterization.

Appendix A
Nominal Error Models

$$\mathbf{C}_{\text{int}}(l,l) = \sigma^2_{\text{URA},l} + \sigma^2_{\text{iono},l} + \sigma^2_{\text{tropo},l} + \sigma_{\text{user},l},$$
$$\mathbf{C}_{\text{acc}}(l,l) = \sigma^2_{\text{URE},l} + \sigma^2_{\text{iono},l} + \sigma^2_{\text{tropo},l} + \sigma_{\text{user},l},$$

where $\sigma_{\text{URE},l}$ is the standard deviation of the clock and ephemeris error of GNSS satellite l used for accuracy and continuity; $\sigma_{\text{URE},l}$ is different from $\sigma_{\text{URA},l}$ in the sense that $\sigma_{\text{URE},l}$ is the average, other than overbounding standard deviation of the nominal errors; $\sigma_{\text{iono},l}$ and $\sigma_{\text{tropo},l}$ denote the standard deviation of the residual ionospheric and tropospheric errors, respectively; and $\sigma_{\text{user},l}$ denotes the standard deviation of the code noise and multipath errors. Terrestrial SOPs are not influenced by ionospheric and tropospheric delays. Therefore, the nominal error models for terrestrial SOPs do not contain $\sigma_{\text{iono},l}$ and $\sigma_{\text{tropo},l}$. For dual-frequency GNSS receivers, the ionospheric delay in the pseudorange measurements can be completely eliminated by dual-frequency. Therefore, the error models do not contain the residual ionospheric delay.

Appendix B
Calculation of Fault Mode Probability

The calculation of fault mode probability $P_{\text{f}}^{(i)}, i \in \{1,\ldots,N_{\text{f}}\}$ is performed using the probabilities of single-ranging-source fault and the probabilities of constellation-wide fault as described in [32]. Suppose there are a total of N_s GNSS satellites and/or SOP towers available in the environment, belonging to N_{const} constellations. The probability of single-ranging-source fault is denoted by $P_{s,m}, m \in \{1,\ldots,N_{\text{s}}\}$. The probability of constellation-wide fault is denoted by $P_{\text{const},n}, n \in \{1,\ldots,N_{\text{const}}\}$. To generalize the notations, the single-ranging-source faults and constellation-wide faults are unified into events, i.e.,

$$P_{\text{event},m} = P_{\text{s},m}, \quad m \in \{i,\ldots,N_{\text{s}}\}$$
$$P_{\text{event},N_{\text{s}}+n} = P_{\text{const},n} \quad n \in \{i,\ldots,N_{\text{const}}\}.$$

The probability of fault mode i is given by

$$P_{\text{f}}^{(i)} = \prod_{l}^{N_{\text{s}}+N_{\text{const}}} P_{\text{event},l}^{B_{l,i}} \left(1 - P_{\text{event},l}\right)^{B_{l,i}}, \tag{17}$$

where

$$B_{l,i} = \begin{cases} 1, & \text{if event } l \text{ is in fault mode } i \\ 0, & \text{otherwise.} \end{cases}$$

Appendix C
Proof of Theorem 1

Proof: Assume that M_{s} pseudorange measurements and WNLS be formulated as discussed in Section III. After adding one pseudorange measurement, the number of fault modes to be monitored will increase by 1, i.e.,

$$N'_{\text{f}} = N_{\text{f}} + 1.$$

Without loss of generality, assume that the N_{f} fault modes correspond to these where one of the original single measurements or constellations is faulty, i.e., for $i = 1,\ldots,N_{\text{f}}$, the measurement vector

$$\boldsymbol{z}^{(i)\prime} = \left[\boldsymbol{z}^{(i)\mathsf{T}}, z_{\text{S}}\right]^{\mathsf{T}},$$

where $\boldsymbol{z}^{(i)\prime}$ and $\boldsymbol{z}^{(i)}$ are the measurement vectors for the new and old systems, respectively, and z_{S} is the additional SOP pseudorange measurement.

One can notice that the measurement vector of the $(N_{\text{f}}+1)$-th fault mode from the new system is identical to the all-in-view measurement vector from the old system, i.e.,

$$\boldsymbol{z}^{(N_{\text{f}}+1)\prime} = \boldsymbol{z}^{(0)}.$$

Based on Theorem III.3 in [19], the addition of a measurement while augmenting the clock state vector by one state

will not improve the position estimate nor the position error uncertainty, i.e., for $i = 0, \ldots, N_{\mathrm{f}}$,

$$\hat{\boldsymbol{x}}^{(i)\prime} = \hat{\boldsymbol{x}}^{(i)}, \tag{18}$$

$$\sigma_q^{(i)\prime} = \sigma_q^{(i)}. \tag{19}$$

It can be readily shown that for $i = 0, \ldots, N_{\mathrm{f}}$

$$\hat{x}_q^{(i)\prime} - \hat{x}_q^{(0)\prime} = \hat{x}_q^{(i)} - \hat{x}_q^{(0)}, \tag{20}$$

$$\sigma_{\mathrm{ss},q}^{(i)\prime} = \sigma_{\mathrm{ss},q}^{(i)}. \tag{21}$$

The test threshold coefficients from (12) for the new system become

$$\begin{aligned} K'_{\mathrm{fa},1} = K'_{\mathrm{fa},2} &= Q^{-1}\left[\frac{P_{\mathrm{FA\_H}}}{2\,(N_{\mathrm{f}}+1)}\right] \\ &> K_{\mathrm{fa},1} = K_{\mathrm{fa},2}, \\ K'_{\mathrm{fa},3} &= Q^{-1}\left[\frac{P_{\mathrm{FA\_V}}}{2\,(N_{\mathrm{f}}+1)}\right] > K_{\mathrm{fa},3}. \end{aligned}$$

The above inequality uses the fact that the inverse Q function is monotonically decreasing. Therefore,

$$T'_{i,q} > T_{i,q}, \quad \text{for } i = 1, \ldots, N_{\mathrm{f}}. \tag{22}$$

Combining the above with (20) yields

$$\frac{\left|\hat{x}_q^{(i)\prime} - \hat{x}_q^{(0)\prime}\right|}{T'_{i,q}} < \frac{\left|\hat{x}_q^{(i)} - \hat{x}_q^{(0)}\right|}{T_{i,q}}, \quad \text{for } i = 1, \ldots, N_{\mathrm{f}}.$$

This means that the new system is less sensitive to faults from the original constellations. Recall from (13) that $\tau_{i,q} = \frac{|\hat{x}_q^{(i)} - \hat{x}_q^{(0)}|}{T_{i,q}}$ is compared to 1 as the fault detection test.

For the fault mode corresponding to the new measurement,

$$\hat{\boldsymbol{x}}^{(N_{\mathrm{f}}+1)\prime} = \hat{\boldsymbol{x}}^{(0)\prime}$$

Therefore, for $q = 1, 2, 3$,

$$|\hat{x}_q^{(N_{\mathrm{f}}+1)\prime} - \hat{x}_q^{(0)\prime}| = 0 < T'_{N_{\mathrm{f}}+1,q}$$

will always hold. This means the new system cannot detect faults from the additional constellation.

□

APPENDIX D
PROOF OF THEOREM 2

Proof: The proof of this theorem will first consider PL_3 (VPL). From Theorem III.3 in [19], it can be readily shown that

$$\mathbf{S}^{(i)\prime} = \begin{cases} \left[\mathbf{S}^{(i)}, \mathbf{0}\right] & i = 0, \ldots, N_{\mathrm{f}} \\ \mathbf{S}^{(0)} & i = N_{\mathrm{f}}+1. \end{cases}$$

Assume unimodal overbounding of the nominal error for the additional pseudorange, i.e., $b_{\mathrm{nom},j} = 0$ for $j = M_{\mathrm{s}}+1$. It can readily shown that the worst-case bias of the new system for the fault modes corresponding to the original measurements ($i = 1, \ldots, N_{\mathrm{f}}$)

$$b_q^{(i)\prime} = \sum_{j=1}^{M_{\mathrm{s}}+1} \left|\mathbf{S}_{q,j}^{(i)\prime}\right| b_{\mathrm{nom},j} = \sum_{j=1}^{M_{\mathrm{s}}} \left|\mathbf{S}_{q,j}^{(i)}\right| b_{\mathrm{nom},j} = b_q^{(i)}. \tag{23}$$

For the fault mode corresponding to the new measurement

$$b_q^{(N_{\mathrm{f}}+1)\prime} = \sum_{j=1}^{M_{\mathrm{s}}+1} \left|\mathbf{S}_{q,j}^{(N_{\mathrm{f}}+1)\prime}\right| b_{\mathrm{nom},j} = \sum_{j=1}^{M_{\mathrm{s}}} \left|\mathbf{S}_{q,j}^{(i)}\right| b_{\mathrm{nom},j} = b_q^{(0)}. \tag{24}$$

First, assume the probability of single fault for the additional measurement $P_{\mathrm{s,new}} = 0$. For $i = 1, \ldots, N_{\mathrm{f}}$,

$$P_{\mathrm{f}}^{(i)\prime} = P_{\mathrm{f}}^{(i)}. \tag{25}$$

For $i = N_{\mathrm{f}} + 1$, one also has

$$P_{\mathrm{f}}^{(N_{\mathrm{f}}+1)\prime} = 0. \tag{26}$$

The probability of fault modes not monitored

$$P'_{\mathrm{NM}} = P_{\mathrm{NM}}. \tag{27}$$

Substituting (19) and (23)-(27) into (16), the equation to compute VPL for the new system with P_{new} becomes

$$\begin{aligned} &2Q\left(\frac{PL'_{3,0} - b_3^{(0)}}{\sigma_3^{(0)}}\right) + \sum_{i=1}^{N_{\mathrm{f}}} P_{\mathrm{f}}^{(i)} Q\left(\frac{PL'_{3,0} - T'_{i,3} - b_3^{(i)}}{\sigma_3^{(i)}}\right) \\ &\quad = PHMI_V\left(1 - \frac{P_{\mathrm{NM}}}{PHMI_V + PHMI_H}\right). \end{aligned} \tag{28}$$

Considering inequality (22) and the monotonicity of the Q function yields that the computed VPL for $P_{\mathrm{s,new}} = 0$,

$$PL'_{3,0} > PL_3. \tag{29}$$

This means that adding one measurement with the probability of fault $P_{\mathrm{s,new}} = 0$ from an additional constellation will increase the computed VPL.

Second, the case when $P_{\mathrm{s,new}} > 0$ is considered. Without loss of generality, assume the same probability of narrow fault $P_{\mathrm{s,old}}$ for all the previous ranging sources and the probability of wide fault to be 0 for all the previous ranging constellations. The probability of fault modes not monitored for the new system can be given by

$$\begin{aligned} P'_{\mathrm{NM}} &= 1 - \sum_{i=0}^{N_{\mathrm{f}}+1} P_{\mathrm{f}}^{(i)\prime} \\ &= 1 - (1 - P_{\mathrm{s,old}})^{M_{\mathrm{s}}} - M_{\mathrm{s}}(1 - P_{\mathrm{s,old}})^{M_{\mathrm{s}}-1} P_{\mathrm{s,old}} \\ &\quad + P_{\mathrm{new}} M_{\mathrm{s}}(1 - P_{\mathrm{s,old}})^{M_{\mathrm{s}}-1} P_{\mathrm{s,old}} \end{aligned}$$

Let $x = PL'_3$, $y = P_{\mathrm{s,new}}$, and

$$\begin{aligned} f(x, y) &= 2Q\left(\frac{PL'_3 - b_3^{(0)\prime}}{\sigma_3^{(0)\prime}}\right) \\ &\quad + \sum_{i=1}^{N_{\mathrm{f}}+1} P_{\mathrm{f}}^{(i)\prime} Q\left(\frac{PL'_3 - T'_{i,3} - b_3^{(i)\prime}}{\sigma_3^{(i)\prime}}\right) \\ &\quad - PHMI_{\mathrm{V}}\left(1 - \frac{P'_{\mathrm{NM}}}{PHMI_{\mathrm{V}} + PHMI_{\mathrm{H}}}\right) \end{aligned}$$

$$f(x, y) = 2Q\left(\frac{x - b_3^{(0)}}{\sigma_3^{(0)}}\right) + y\left(1 - P_{\mathrm{s,old}}\right)^M Q\left(\frac{x - b_3^{(0)}}{\sigma_3^{(0)}}\right)$$

$$+ (1-y)\sum_{i=1}^{N_{\mathrm{f}}} P_{\mathrm{f}}^{(i)} Q\left(\frac{x - T'_{i,3} - b_3^{(i)}}{\sigma_3^{(i)}}\right) + y \cdot a \cdot M_{\mathrm{s}}(1-P_{\mathrm{s,old}})^{M_{\mathrm{s}}-1} P_{\mathrm{s,old}} - PHMI'_{\mathrm{V}}, \tag{30}$$

where

$$a = \frac{PHMI_{\mathrm{V}}}{PHMI_{\mathrm{V}} + PHMI_{\mathrm{H}}},$$
$$PHMI'_{\mathrm{V}} = PHMI_V\left[1 - \frac{d}{PHMI_{\mathrm{V}} + PHMI_{\mathrm{H}}}\right],$$
$$d = 1 - \left(1 - P_{\mathrm{s,old}}\right)^M - M\left(1 - P_{\mathrm{s,old}}\right)^{M-1} P_{\mathrm{s,old}}.$$

Considering that the Q function is monotonically decreasing, it can be readily shown that $f_x < 0$, where f_x denotes the derivative of $f(x, y)$ with respect to x. Taking derivative of $f(x, y)$ with respect to y yields

$$f_y = a \cdot M_{\mathrm{s}}(1-P_{\mathrm{s,old}})^{M_{\mathrm{s}}-1} P_{\mathrm{s,old}} + (1-P_{\mathrm{s,old}})^{M_{\mathrm{s}}} Q\left(\frac{x - b_3^{(0)}}{\sigma_3^{(0)}}\right) - (1-P_{\mathrm{s,old}})^{M_{\mathrm{s}}-1} P_{\mathrm{s,old}} \sum_{i=1}^{M_{\mathrm{s}}} Q\left(\frac{x - T'_{i,3} - b_3^{(i)}}{\sigma_3^{(i)}}\right) \tag{31}$$

Under baseline specifications, the first term dominates the above equation. Therefore

$$f_y > 0.$$

Letting $f(x, y) = 0$ and taking the total derivative yields

$$\frac{dx}{dy} = -\frac{f_y}{f_x} > 0$$

This indicates that PL'_3 increases with P_{new} increasing. Therefore,

$$PL'_3 > PL'_{3,0} > PL_3 \tag{32}$$

Using similar steps, the same conclusion can be achieved for the two horizontal directions. □

REFERENCES

[1] R. Sabatini et al., "Avionics systems panel research and innovation perspectives," *IEEE Aerosp. Electron. Syst. Mag.*, vol. 35, no. 12, pp. 58–72, Dec. 2020.

[2] A. Schütz, D. E. Sánchez-Morales, and T. Pany, "Precise positioning through a loosely-coupled sensor fusion of GNSS-RTK, INS and LiDAR for autonomous driving," in *Proc. IEEE/ION Position, Location Navigat. Symp. (PLANS)*, Apr. 2020, pp. 219–225.

[3] D. Imparato, A. El-Mowafy, and C. Rizos, "Integrity monitoring: From airborne to land applications," in *Multifunctional Operation and Application of GPS*. London, U.K.: IntechOpen, 2018, pp. 23–43.

[4] X. Wang, C. Toth, and D. Grejner-Brzezinska, "A survey on integrity monitoring of GNSS navigation for ground vehicles," in *Proc. 34th Int. Tech. Meeting Satell. Division Inst. Navigat. (ION GNSS)*, Oct. 2021, pp. 2591–2601.

[5] F. A. C. de Oliveira, F. S. Torres, and A. García-Ortiz, "Recent advances in sensor integrity monitoring methods—A review," *IEEE Sensors J.*, vol. 22, no. 11, pp. 10256–10279, Jun. 2022.

[6] J. Raquet et al., "Part D: Position, navigation, and timing using radio signals-of-opportunity," in *Position, Navigation, and Timing Technologies in the 21st Century*, vol. 2, J. Morton, F. van Diggelen, J. Spilker Jr., and B. Parkinson, Eds. Hoboken, NJ, USA: Wiley, 2021, chs. 35–43, pp. 1115–1412.

[7] N. Souli, R. Makrigiorgis, P. Kolios, and G. Ellinas, "Real-time relative positioning system implementation employing signals of opportunity, inertial, and optical flow modalities," in *Proc. Int. Conf. Unmanned Aircr. Syst. (ICUAS)*, Jun. 2021, pp. 229–236.

[8] K. Strandjord, Y. J. Morton, and P. Wang, "Evaluating the urban signal environment for GNSS and LTE signals," in *Proc. 34th Int. Tech. Meeting Satell. Division Inst. Navigat. (ION GNSS)*, Oct. 2021, pp. 2166–2182.

[9] M. Maaref and Z. Kassas, "Ground vehicle navigation in GNSS-challenged environments using signals of opportunity and a closed-loop map-matching approach," *IEEE Trans. Intell. Transp. Syst.*, vol. 21, no. 7, pp. 2723–2738, Jul. 2020.

[10] C. Yang, M. Arizabaleta-Diez, P. Weitkemper, and T. Pany, "An experimental analysis of cyclic and reference signals of 4G LTE for TOA estimation and positioning in mobile fading environments," *IEEE Aerosp. Electron. Syst. Mag.*, vol. 37, no. 9, pp. 16–41, Sep. 2022.

[11] N. Souli, P. Kolios, and G. Ellinas, "Online relative positioning of autonomous vehicles using signals of opportunity," *IEEE Trans. Intell. Vehicles*, vol. 7, no. 4, pp. 873–885, Dec. 2022.

[12] Z. Jiao et al., "Carrier phase ranging with DTMB signals for urban pedestrian localization and GNSS aiding," *Remote Sens.*, vol. 15, no. 2, pp. 423–446, 2023.

[13] X. Chen, Q. Wei, F. Wang, Z. Jun, S. Wu, and A. Men, "Super-resolution time of arrival estimation for a symbiotic FM radio data system," *IEEE Trans. Broadcast.*, vol. 66, no. 4, pp. 847–856, Dec. 2020.

[14] M. L. Psiaki and B. D. Slosman, "Tracking digital FM OFDM signals for the determination of navigation observables," *Navigat., J. Inst. Navigat.*, vol. 69, no. 2, 2022, Art. no. navi.521.

[15] R. X. T. Kor, P. A. Iannucci, and T. E. Humphreys, "Autonomous signal-situational-awareness in a terrestrial radionavigation system," in *Proc. IEEE Int. Intell. Transp. Syst. Conf. (ITSC)*, Sep. 2021, pp. 3965–3971.

[16] Y. Hao, M. Chen, L. Hu, J. Song, M. Volk, and I. Humar, "Wireless fractal ultra-dense cellular networks," *Sensors*, vol. 17, no. 4, pp. 847–853, 2017.

[17] M. Maaref, J. Khalife, and Z. Kassas, "Aerial vehicle protection level reduction by fusing GNSS and terrestrial signals of opportunity," *IEEE Trans. Intell. Transp. Syst.*, vol. 22, no. 9, pp. 5976–5993, Sep. 2021.

[18] *Evolved Universal Terrestrial Radio Access (E-UTRA); Requirements for Support of Radio Resource Management*, document TS 36.133, 3GPP, Apr. 2010. [Online]. Available: https://www.3gpp.org/dynareport/36133.htm

[19] J. Khalife and Z. Kassas, "On the achievability of submeter-accurate UAV navigation with cellular signals exploiting loose network synchronization," *IEEE Trans. Aerosp. Electron. Syst.*, vol. 58, no. 5, pp. 4261–4278, Oct. 2022.

[20] N. Zhu, J. Marais, D. Bétaille, and M. Berbineau, "GNSS position integrity in urban environments: A review of literature," *IEEE Trans. Intell. Transp. Syst.*, vol. 19, no. 9, pp. 2762–2778, Sep. 2018.

[21] B. Belabbas, P. Remi, and M. Meurer, "Performance assessment of GBAS CAT III using GPS and Galileo," in *Proc. ION GNSS Conf.*, Sep. 2008, pp. 2945–2952.

[22] R. Sabatini, T. Moore, and C. Hill, "Avionics-based GNSS integrity augmentation synergies with SBAS and GBAS for safety-critical aviation applications," in *Proc. IEEE/AIAA 35th Digit. Avionics Syst. Conf. (DASC)*, Sep. 2016, pp. 1–10.

[23] J. Blanch, T. Walter, Y. Lee, B. Pervan, M. Rippl, and A. Spletter, "Advanced RAIM user algorithm description: Integrity support message processing, fault detection, exclusion, and protection level calculation," in *Proc. ION GNSS Conf.*, Sep. 2012, pp. 2828–2849.

[24] J. Blanch et al., "Critical elements for a multi-constellation advanced RAIM," *Navigat., J. Inst. Navigat.*, vol. 60, no. 1, pp. 53–69, 2013.

[25] A. Ene, J. Blanch, and T. Walter, "Galileo-GPS RAIM for vertical guidance," in *Proc. Nat. Tech. Meeting Inst. Navigat.*, Jan. 2006, pp. 18–20.

[26] T. Walter, J. Blanch, M. J. Choi, T. Reid, and P. Enge, "Incorporating GLONASS into aviation RAIM receivers," in *Proc. Int. Tech. Meeting Inst. Navigat.*, Jan. 2013, pp. 239–249.

[27] Y. Liu, J. Zhang, R. Xue, and Z. Wang, "Performance analysis of advanced RAIM with the inclusion of BeiDou," in *Proc. ION Int. Tech. Meeting*, 2014, pp. 3629–3636.

[28] P. F. Roysdon and J. A. Farrell, "GPS-INS outlier detection & elimination using a sliding window filter," in *Proc. Amer. Control Conf. (ACC)*, May 2017, pp. 1244–1249.

[29] T. Li et al., "P3-LOAM: PPP/LiDAR loosely coupled SLAM with accurate covariance estimation and robust RAIM in urban canyon environment," *IEEE Sensors J.*, vol. 21, no. 5, pp. 6660–6671, Mar. 2021.

[30] L. Fu, J. Zhang, R. Li, X. Cao, and J. Wang, "Vision-aided RAIM: A new method for GPS integrity monitoring in approach and landing phase," *Sensors*, vol. 15, no. 9, pp. 22854–22873, Sep. 2015.

[31] FAA GEAS Panel. *Phase II of the GNSS Evolutionary Architecture Study*. Accessed: Feb. 2010. [Online]. Available: http://www.faa.gov/about/officeorg/headquartersoffices/ato?/serviceunits/techops/navservices/gnss/library/documents/media/GEASPhaseIIFinal.pdf

[32] *Advanced RAIM Technical Subgroup Reference Airborne Algorithm Description Document*, document, 3GPP, Working Group-C (WG-C), Jun. 2019. [Online]. Available: http://web.stanford.edu/group/scpnt/gpslab/websitefiles/maast/ARAIM TSG Reference ADD v3.1.pdf

[33] J. Blanch, T. Walter, and P. Enge, "RAIM with optimal integrity and continuity allocations under multiple failures," *IEEE Trans. Aerosp. Electron. Syst.*, vol. 46, no. 3, pp. 1235–1247, Jul. 2010.

[34] M. Joerger, S. Stevanovic, S. Langel, and B. Pervan, "Integrity risk minimisation in RAIM Part 1: Optimal detector design," *Navig. J. Inst. Navig.*, vol. 69, no. 3, pp. 449–467, May 2016.

[35] M. Joerger, S. Stevanovic, S. Langel, and B. Pervan, "Integrity risk minimisation in RAIM Part 2: Optimal detector design," *Navig. J. Inst. Navig.*, vol. 69, no. 4, pp. 709–728, 2016.

[36] M. Joerger, Y. Zhai, I. Martini, J. Blanch, and B. Pervan, "ARAIM continuity and availability assertions, assumptions, and evaluation methods," in *Proc. Int. Tech. Meeting Inst. Navigat.*, Feb. 2020, pp. 404–420.

[37] Y. Zhai, X. Zhan, J. Chang, and B. Pervan, "ARAIM with more than two constellations," in *Proc. ION Pacific PNT Meeting*, May 2019, pp. 925–941.

[38] X. Zheng, Y. Liu, G. Guan, J. Zhao, and C. Xu, "Analyses of the sensitivity of multi-constellation advanced receiver autonomous integrity monitoring vertical protection level availability to error parameters and a failure model over China," *Adv. Mech. Eng.*, vol. 10, no. 6, pp. 1–11, 2018.

[39] Z. Madadi, F. Quitin, and W. P. Tay, "Receiver tracking using signals of opportunity from asynchronous RF beacons in GNSS-denied environments," in *Proc. IEEE 84th Veh. Technol. Conf. (VTC-Fall)*, Sep. 2016, pp. 1–5.

[40] N. Ikhtiari, "Navigation in GNSS denied environments using software defined radios and LTE signals of opportunities," M.S. thesis, Air Force Inst. Technol., Wright-Patterson Air Force Base, OH, USA, 2019.

[41] N. Souli, P. Kolios, and G. Ellinas, "Relative positioning of autonomous systems using signals of opportunity," in *Proc. IEEE 91st Veh. Technol. Conf. (VTC-Spring)*, May 2020, pp. 1–6.

[42] N. Jardak and Q. Jault, "The potential of LEO satellite-based opportunistic navigation for high dynamic applications," *Sensors*, vol. 22, no. 7, pp. 2541–2565, 2022.

[43] Z. Kassas, M. Maaref, J. Morales, J. Khalife, and K. Shamei, "Robust vehicular localization and map matching in urban environments through IMU, GNSS, and cellular signals," *IEEE Intell. Transp. Syst. Mag.*, vol. 12, no. 3, pp. 36–52, Fall. 2020.

[44] Z. Kassas, J. Khalife, A. Abdallah, and C. Lee, "I am not afraid of the GPS jammer: Resilient navigation via signals of opportunity in GPS-denied environments," *IEEE Aerosp. Electron. Syst. Mag.*, vol. 37, no. 7, pp. 4–19, Jul. 2022.

[45] M. Maaref, J. Khalife, and Z. Kassas, "Lane-level localization and mapping in GNSS-challenged environments by fusing LiDAR data and cellular pseudoranges," *IEEE Trans. Intell. Vehicles*, vol. 4, no. 1, pp. 73–89, Mar. 2019.

[46] J. Morales and Z. Kassas, "Tightly coupled inertial navigation system with signals of opportunity aiding," *IEEE Trans. Aerosp. Electron. Syst.*, vol. 57, no. 3, pp. 1930–1948, Jun. 2021.

[47] H. Dun, C. C. J. M. Tiberius, and G. J. M. Janssen, "Positioning in a multipath channel using OFDM signals with carrier phase tracking," *IEEE Access*, vol. 8, pp. 13011–13028, 2020.

[48] P. Wang and Y. J. Morton, "Performance comparison of time-of-arrival estimation techniques for LTE signals in realistic multipath propagation channels," *Navigat., J. Inst. Navigat.*, vol. 67, no. 4, pp. 691–712, Dec. 2020.

[49] P. Wang and Y. J. Morton, "Multipath estimating delay lock loop for LTE signal TOA estimation in indoor and urban environments," *IEEE Trans. Wireless Commun.*, vol. 19, no. 8, pp. 5518–5530, Aug. 2020.

[50] T. Kazaz, G. Janssen, J. Romme, and A. Van der Veen, "Delay estimation for ranging and localization using multiband channel state information," *IEEE Trans. Wireless Commun.*, vol. 21, no. 4, pp. 2591–2607, Apr. 2022.

[51] A. Abdallah and Z. Kassas, "Multipath mitigation via synthetic aperture beamforming for indoor and deep urban navigation," *IEEE Trans. Veh. Technol.*, vol. 70, no. 9, pp. 8838–8853, Sep. 2021.

[52] Z. Kassas et al., "Assessment of cellular signals of opportunity for high-altitude aircraft navigation," *IEEE Aerosp. Electron. Syst. Mag.*, vol. 37, no. 10, pp. 4–19, Oct. 2022.

[53] Z. Kassas et al., "Flight demonstration of high altitude aircraft navigation with cellular signals," *IEEE Intell. Transp. Syst. Mag.*, vol. 15, no. 4, pp. 150–165, Oct. 2023.

[54] J. Gante, L. Sousa, and G. Falcao, "Dethroning GPS: Low-power accurate 5G positioning systems using machine learning," *IEEE J. Emerg. Sel. Topics Circuits Syst.*, vol. 10, no. 2, pp. 240–252, Jun. 2020.

[55] K. Shamaei and Z. Kassas, "Receiver design and time of arrival estimation for opportunistic localization with 5G signals," *IEEE Trans. Wireless Commun.*, vol. 20, no. 7, pp. 4716–4731, Jul. 2021.

[56] L. Chen, X. Zhou, F. Chen, L. Yang, and R. Chen, "Tracking digital FM OFDM signals for the determination of navigation observables," *IEEE Internet Things J.*, vol. 9, no. 13, pp. 10908–10919, 2022.

[57] A. Abdallah and Z. Kassas, "UAV navigation with 5G carrier phase measurements," in *Proc. 34th Int. Tech. Meeting Satell. Division Inst. Navigat. (ION GNSS)*, Oct. 2021, pp. 3294–3306.

[58] A. Abdallah and Z. Kassas, "Opportunistic navigation using sub-6 GHz 5G downlink signals: A case study on a ground vehicle," in *Proc. 16th Eur. Conf. Antennas Propag. (EuCAP)*, Mar. 2022, pp. 1–5.

[59] A. Abdallah, J. Khalife, and Z. Kassas, "Exploiting on-demand 5G downlink signals for opportunistic navigation," *IEEE Signal Process. Lett.*, vol. 30, pp. 389–393, 2023.

[60] M. Jia, J. Khalife, and Z. Kassas, "Evaluation of ground vehicle protection level reduction due to fusing GPS with faulty terrestrial signals of opportunity," in *Proc. Int. Tech. Meeting Inst. Navigat.*, Feb. 2021, pp. 354–365.

[61] M. Jia, H. Lee, J. Khalife, Z. Kassas, and J. Seo, "Ground vehicle navigation integrity monitoring for multi-constellation GNSS fused with cellular signals of opportunity," in *Proc. IEEE Int. Intell. Transp. Syst. Conf. (ITSC)*, Sep. 2021, pp. 3978–3983.

[62] M. Maaref and Z. Kassas, "Measurement characterization and autonomous outlier detection and exclusion for ground vehicle navigation with cellular signals," *IEEE Trans. Intell. Vehicles*, vol. 5, no. 4, pp. 670–683, Dec. 2020.

[63] M. Maaref and Z. Kassas, "Autonomous integrity monitoring for vehicular navigation with cellular signals of opportunity and an IMU," *IEEE Trans. Intell. Transp. Syst.*, vol. 23, no. 6, pp. 5586–5601, Jun. 2022.

[64] E. Kaplan and C. Hegarty, *Understanding GPS: Principles and Applications*, 2nd ed. Norwood, MA, USA: Artech House, 2005.

[65] J. Khalife and Z. Kassas, "Evaluation of relative clock stability in cellular networks," in *Proc. 30th Int. Tech. Meeting Satell. Division Inst. Navigat. (ION GNSS)*, Nov. 2017, pp. 2554–2559.

[66] B. DeCleene, "Defining pseudorange integrity-overbounding," in *Proc. Int. Tech. Meeting Satell. Division Inst. Navigat.*, Sep. 2000, pp. 1916–1924.

[67] M. Haenggi, J. G. Andrews, F. Baccelli, O. Dousse, and M. Franceschetti, "Stochastic geometry and random graphs for the analysis and design of wireless networks," *IEEE J. Sel. Areas Commun.*, vol. 27, no. 7, pp. 1029–1046, Sep. 2009.

[68] J. Khalife, C. Sevinc, and Z. Kassas, "Performance evaluation of TOA positioning in asynchronous cellular networks using stochastic geometry models," *IEEE Wireless Commun. Lett.*, vol. 9, no. 9, pp. 1422–1426, Sep. 2020.

[69] S. Aditya, H. S. Dhillon, A. F. Molisch, R. M. Buehrer, and H. M. Behairy, "Characterizing the impact of SNR heterogeneity on time-of-arrival-based localization outage probability," *IEEE Trans. Wireless Commun.*, vol. 18, no. 1, pp. 637–649, Jan. 2019.

[70] J. Blanch et al., "Baseline advanced RAIM user algorithm and possible improvements," *IEEE Trans. Aerosp. Electron. Syst.*, vol. 51, no. 1, pp. 713–732, Jan. 2015.

[71] T. Walter, J. Blanch, K. Gunning, M. Joerger, and B. Pervan, "Determination of fault probabilities for ARAIM," *IEEE Trans. Aerosp. Electron. Syst.*, vol. 55, no. 6, pp. 3505–3516, Dec. 2019.

[72] J. Khalife, M. Maaref, and Z. Kassas, "Opportunistic autonomous integrity monitoring for enhanced UAV safety," *IEEE Aerosp. Electron. Syst. Mag.*, vol. 38, no. 5, pp. 34–44, May 2023.

[73] K. Shamaei and Z. Kassas, "LTE receiver design and multipath analysis for navigation in urban environments," *Navigat., J. Inst. Navigat.*, vol. 65, no. 4, pp. 655–675, Dec. 2018.

[74] J. Spilker Jr., "Overview of GPS operation and design," in *Global Positioning System: Theory and Applications*. Washington, DC, USA: American Institute of Aeronautics and Astronautics, 1996, ch. 2, pp. 57–119.

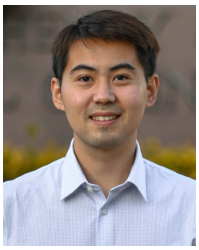

Mu Jia (Graduate Student Member, IEEE) received the B.E. degree in vehicle engineering from Shandong University, the M.E. degree in mechanical engineering from the University of Defense Technology, and the M.S. degree in mechanical engineering from Duke University. He is currently pursuing the Ph.D. degree with The Ohio State University. He is a member of the Autonomous Systems Perception, Intelligence, and Navigation (ASPIN) Laboratory. His current research interests include autonomous vehicles, integrity monitoring, and opportunistic navigation.

Joe Khalife (Student Member, IEEE) received the B.E. degree in electrical engineering and the M.S. degree in computer engineering from Lebanese American University and the Ph.D. degree in electrical engineering and computer science from the University of California at Irvine. He was a Post-Doctoral Fellow with the University of California at Irvine and a member of the ASPIN Laboratory. He was a recipient of the 2016 IEEE/ION Position, Location and Navigation Symposium (PLANS) Best Student Paper Award and the 2018 IEEE Walter Fried Award.

Zaher (Zak) M. Kassas (Senior Member, IEEE) received the B.E. degree in electrical engineering from Lebanese American University, the M.S. degree in electrical and computer engineering from The Ohio State University, and the M.S.E. degree in aerospace engineering and the Ph.D. degree in electrical and computer engineering from The University of Texas at Austin. He is currently a Professor with The Ohio State University, the Director of the ASPIN Laboratory, and the Director of the U.S. Department of Transportation, Center for Automated Vehicle Research with Multimodal Assured Navigation (CARMEN), where he is focusing on navigation resiliency and security of highly automated transportation systems. His research interests include cyber-physical systems, navigation systems, autonomous vehicles, and intelligent transportation systems. He is a fellow of the ION and a Distinguished Lecturer of the IEEE Aerospace and Electronic Systems Society. He was a recipient of the 2018 National Science Foundation (NSF) CAREER Award, the 2018 IEEE Walter Fried Award, the 2018 Institute of Navigation (ION) Samuel Burka Award, the 2019 ION Colonel Thomas Thurlow Award, the 2019 Office of Naval Research (ONR) Young Investigator Program (YIP) Award, and the 2022 Air Force Office of Scientific Research (AFOSR) YIP Award. He is an Associate Editor of the IEEE TRANSACTIONS ON AEROSPACE AND ELECTRONIC SYSTEMS and the IEEE TRANSACTIONS ON INTELLIGENT TRANSPORTATION SYSTEMS.